Wasted photons: Photogeneration yield and charge carrier collection efficiency of hematite photoanodes for photoelectrochemical water splitting

Yifat Piekner[1], David S. Ellis[2], Daniel A. Grave[2,3], Anton Tsyganok[2], Avner Rothschild[1,2]*

[1]The Nancy & Stephen Grand Technion Energy Program (GTEP), Technion – Israel Institute of Technology, Haifa 32000, Israel
 [2]Department of Materials Science and Engineering, Technion – Israel Institute of Technology, Haifa 3200002, Israel
[3]Department of Materials Engineering and Ilse Katz Institute for Nanoscale Science and Technology, Ben Gurion University of the Negev, Be'er Sheva 8410501, Israel

*Email: avnerrot@technion.ac.il

Supplemental Information

Material characterizations

Figure S1. Photographs of the thin (32 nm, a) and ultrathin (7 nm, b) film hematite photoanodes studied in this work. The orange area is coated by hematite and the transparent area is the rest of the sample with bare ITO transparent current collector. The grid spacing is 0.5 cm.
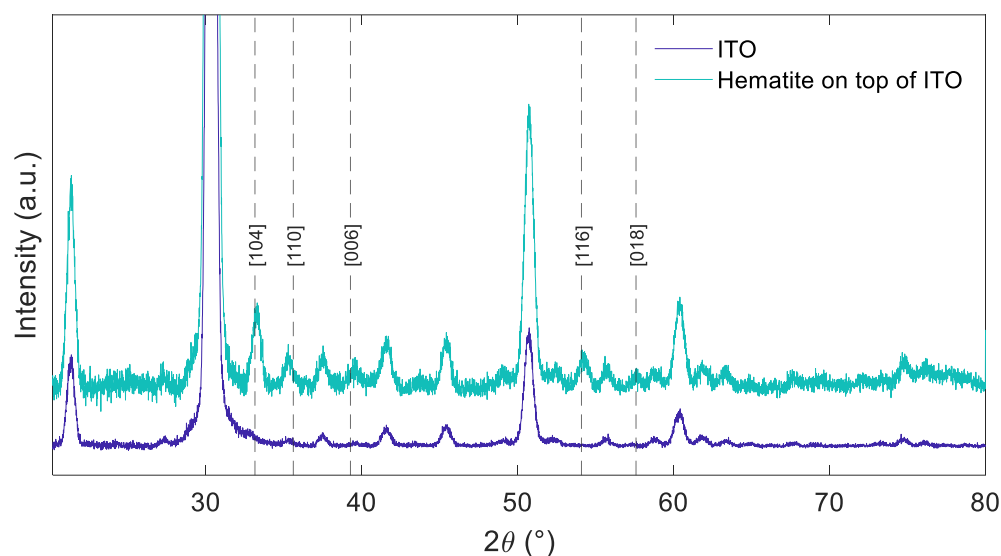

Figure S2. Grazing incidence X-ray diffraction (GIXRD) pattern of the 32 nm thick film hematite photoanode (turquoise), and a bare ITO-coated glass substrate (EAGLE XG glass substrates, Corning) without hematite (blue). The 2θ positions of hematite's Bragg reflections (taken from JCPDS 00-033-0664) are presented by dashed vertical lines with the Miller indices of the corresponding crystallographic planes. The pattern of a bare ITO-coated glass substrate (without hematite) was recorded as well (blue curve, bottom diffractogram) to identify the peaks originated from the ITO layer beneath the hematite.
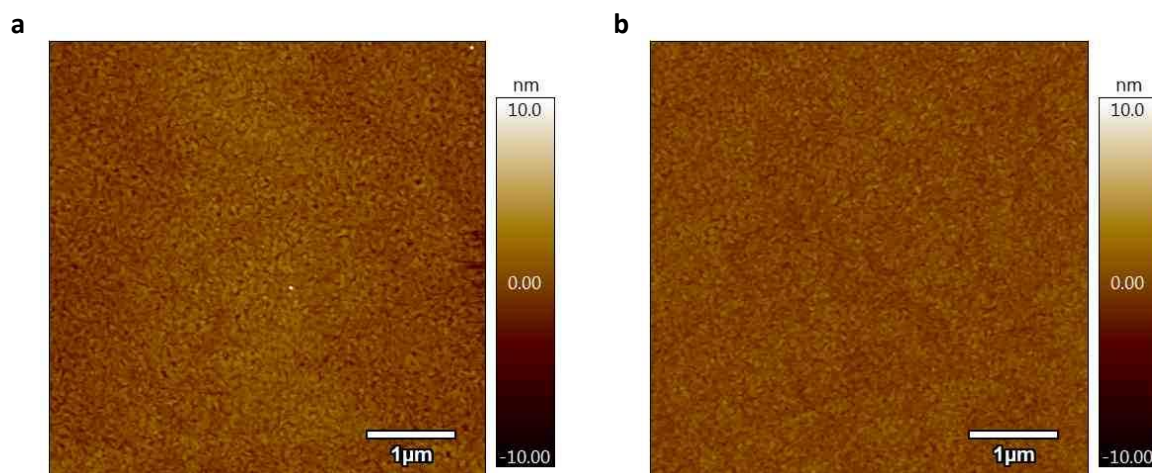

Figure S3. Topographical AFM mapping of the thin (32 nm, a) and ultrathin (7 nm, b) hematite layers comprising the photoanodes studied in this work. The RMS roughness of the thin (a) and ultrathin (b) hematite films was 0.9 and 0.7 nm, respectively.
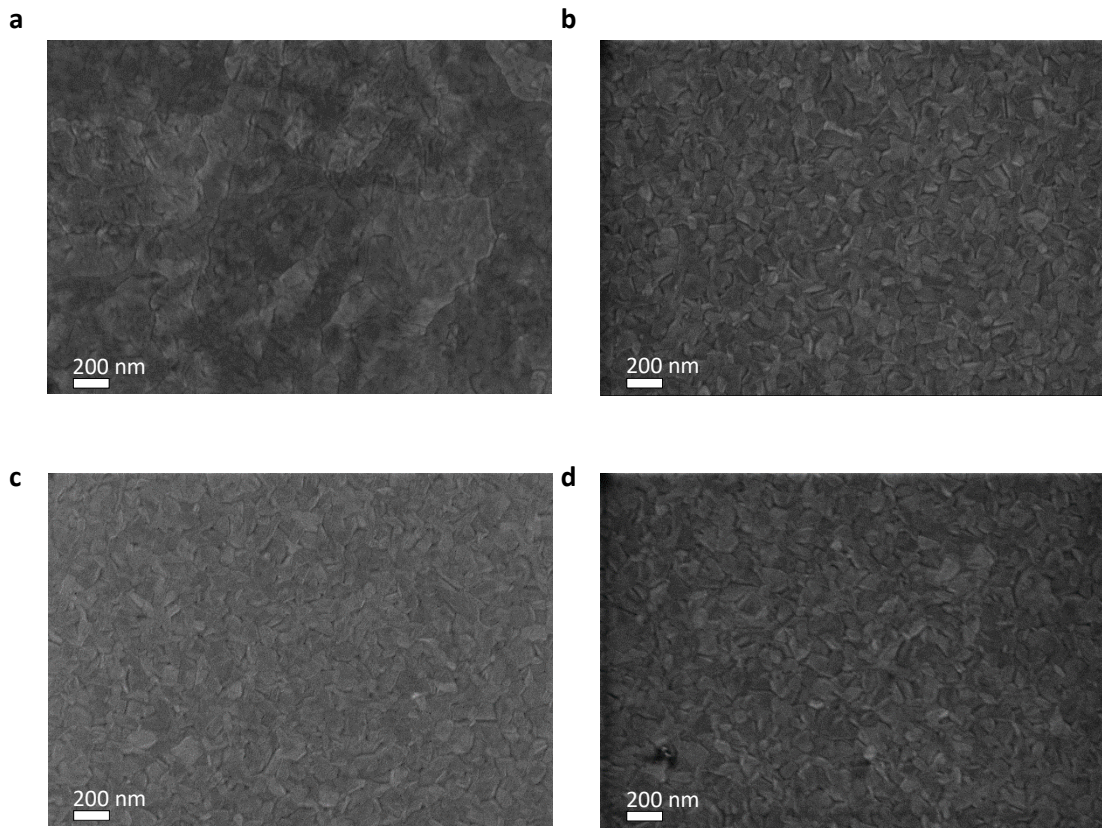
Figure S4. SEM images taken from the hematite (a) and ITO (b) sides of the thin (32 nm) film hematite photoanode presented in Figure S1(a), and from the hematite (c) and ITO (d) sides of the ultrathin (7 nm) film hematite photoanode presented in Figure S1(b).

Ellipsometry analysis

Spectroscopic ellipsometry measures the complex ratio (ρ) between the *p*-polarized (parallel electric field to the plane of incidence) and *s*-polarized (perpendicular electric field to the plane of incidence) reflected light from the sample and presents it in terms of the amplitude ratio, $\tan(\Psi)$, and phase difference, Δ: $\rho = \frac{R_p}{R_s} = \tan(\Psi)e^{i\Delta}$. This measurement can be used to extract the material complex refractive index ($\hat{n}$) using its dependence on the polarization change and the angle of incident (ϕ) expressed by:[1] $(\hat{n})^2 = \sin(\phi)^2 \left[1 + \tan(\phi)^2 \left(\frac{1-\rho}{1+\rho}\right)^2\right]$.

To find the complex refractive indices of the three components comprising the photoanode stack (hematite photoabsorber, ITO current collector and glass substrate), we developed optical models for each one of them. The models rely on ellipsometry measurements of a bare eagle glass substrate, an eagle glass substrate coated with ITO, and a full photoanode stack comprising the substrate coated with ITO and hematite layers. The optical parameters of the bare eagle glass substrate were found using an optical model consisted of seven Gaussian oscillators. The thickness of the substrate was fixed to the nominal value, 1.1 mm, and the other parameters (of the oscillators, poles and offset) were tuned to generate Ψ and Δ spectra that best fit the measured spectra, as presented in Figure S5(a). The mean-squared error (MSE) was 1.561. This model was used, without any alteration, in the analyses of the ITO coated substrate and the full stack photoanode. To analyze the ITO coated substrate, we added to the substrate optical model another layer that was modeled using a superposition of four different types of oscillator functions: Tauc-Lorentz, ρ-τ Drude, Lorentz and Gaussian. The parameters of this layer, including its thickness, were tuned to obtain the best agreement between the measured and generated the Ψ and Δ spectra, as presented in Figure S5(b). The ITO layer thickness was found to be 253 nm, and the MSE was 1.58. The ITO model was used to analyze the full stack photoanode. To account for the hematite layer, another layer, comprised of one Tauc-Lorentz and five Gaussian oscillators, was added. The oscillator parameters and thickness of both the ITO and hematite layers were tuned to obtain the agreement presented in Figure S5(c), with an MSE of 1.759. The 7 nm ultrathin film hematite photoanode was similarly analyzed,[2] except for the hematite layer thickness which was fixed according to cross-section

transmission electron microscopy (TEM), to elude the very strong correlations between the optical parameters and thickness of ultrathin transparent films.

The complex refractive indices corresponding to the ellipsometry model of the 32 nm thick film hematite photoanode are presented in Figure S6(a). Figure S6(b) compares the refractive indices of the 32 and 7 nm thick hematite layers in the photoanodes studied in this work and in our previous work.[2] The blue shift of the primary absorption peak positioned at 400 nm is clearly demonstrated, which we assign to the quantum size effect.[3,4]

Using the optical parameters of the hematite and ITO layers and Eagle glass substrate, we simulated the transmission, reflectance and absorptance spectra of the specimens, and compared the simulated spectra with their empirical counterparts measured by spectrophotometry. The results are presented in Figure S6(a) and S6(b) for the bare Eagle glass substrate and for an Eagle glass substrate coated with a 258 nm thick ITO layer. The comparison between the simulated and measured spectra of the thin (32 nm) film hematite photoanode is presented in Figure 2 in the article, and that of the ultrathin (7 nm) film hematite photoanode is presented in Ref. 2. For these comparisons, we used an incident angle of 5.1° which is the minimal angle enabled by the spectrophotometer, and hence the closest to normal incidence in the EQE measurements. When calculating the absorbed photon flux within the hematite layer under the same conditions as in our EQE measurements, we modeled normal incidence (0° angle) through water as the initial medium. The calculation accounts for different penetration lengths of photons with different wavelengths, as well as resonance effects.
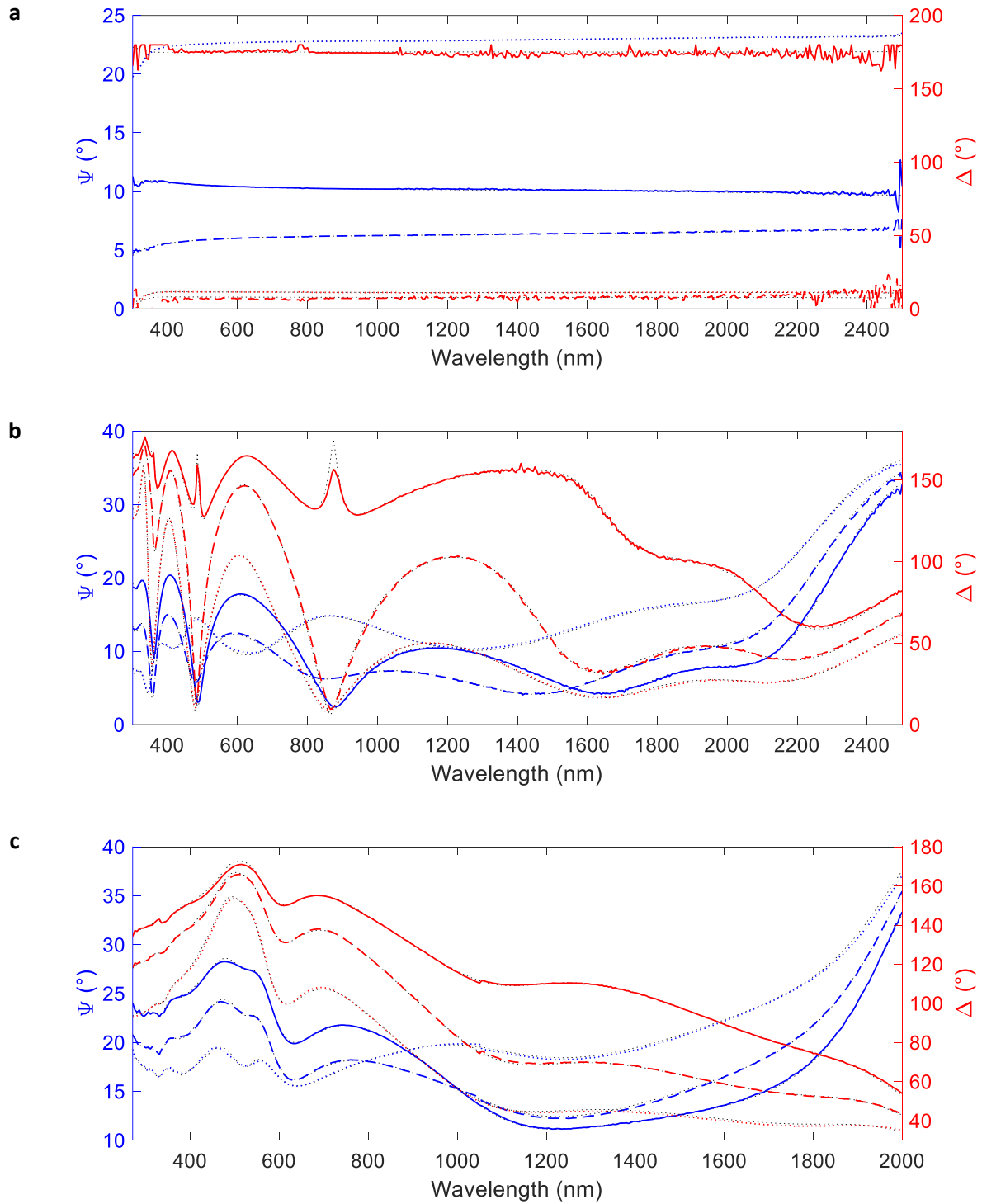
Figure S5. Spectroscopic ellipsometry analysis. The measured Ψ (blue) and Δ (red) spectra and their fitted curves (black dotted lines) of (a) A 1.1 mm thick bare Eagle glass substrate, measured at incidence angles of 50° (solid curve), 60° (dashed curve) and 70° (dotted curve); (b) An Eagle glass substrate coated with a 253 nm thick ITO layer, measured at incidence angles of 55° (solid curve), 60° (dashed curve) and 65° (dotted curve); and (c) A full photoanode stack comprising a 33 nm thick hematite layer deposited on a 269 nm thick ITO-coated Eagle glass substrate (the sample presented in Figure S1(a)), measured at incidence angles of 60° (solid curve), 65° (dashed curve) and 70° (dotted curve).
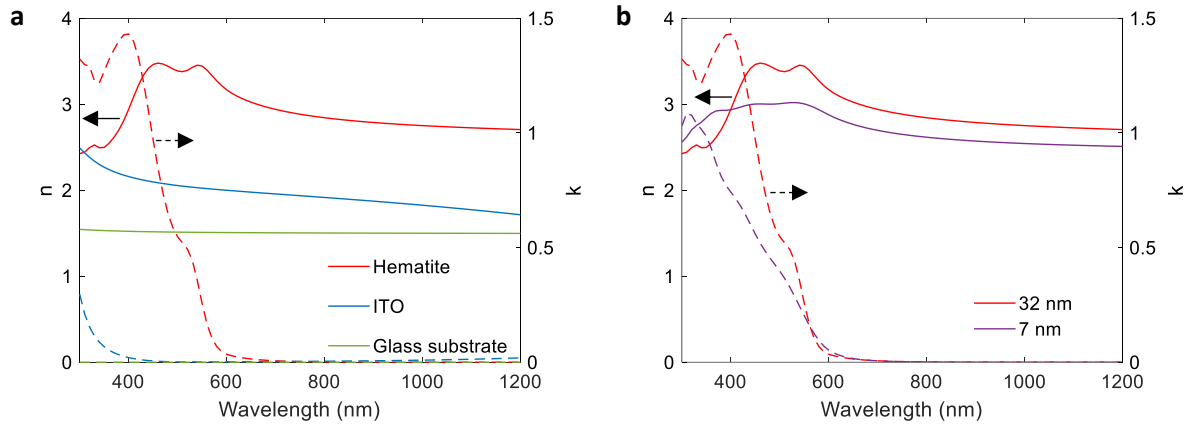
Figure S6. Optical parameters (complex refractive indices) of the photoanode stack components. (a) The real part (*n*, solid lines) and imaginary part (*k*, dashed lines) of the refractive index of the 32 nm thick hematite layer (red), 269 nm thick ITO layer (blue) and 1.1 mm thick Eagle glass substrate (green) comprising the photoanode presented in Figure S1(a). The imaginary part of the refractive index (*k*) of the Eagle glass substrate is close to zero. (b) Comparison between the real (solid lines) and imaginary (dashed lines) parts of the refractive indices of the 32 and 7 nm thick hematite layers (red and purple curves, respectively) of the thin and ultrathin film hematite photoanodes presented in Figure S1(a) and S1(b), respectively.
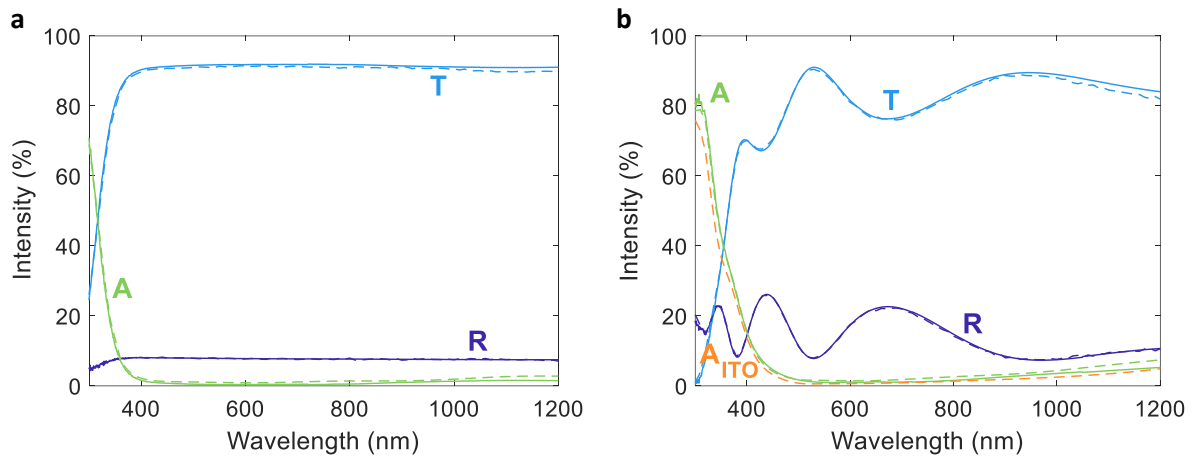

Figure S7. Verification of the glass substrate and the ITO ellipsometry models. Measured (solid lines) and simulated (dashed lines) reflectance (R), transmittance (T) and absorptance (A) spectra of the bare Eagle glass substrate (a), and the 258 nm thick ITO-coated Eagle glass substrate (b), obtained for front illumination in air at an incidence angle of 5.1°. The dashed line orange curve (marked A_{ITO}) presents the simulated absorption within the ITO layer.

Film thickness

The ITO and hematite layers in the thin film hematite photoanode were found to have a thickness of 269 and 33 nm, respectively, by ellipsometry analysis (Figure S5(c)) in a focused measurement point, whose area was ~0.38 mm^2 (700 µm diameter). The ITO layer thickness was found to vary between 253 and 270 nm across the sample, as estimated by ellipsometry mapping of an 8×10 mm^2 measurement area with nine mesh points. The hematite layer thickness was found to vary between 30 and 33.5 nm in the same area. The ellipsometry fitting MSE varied between ~2 to ~19 for different measurement points, suggesting that the thickness found at some points is more accurate than other points. Due to the larger illuminating beam of the spectrophotometer (5x5 mm^2) compared to the ellipsometer, a larger area of the sample was averaged, and hence, the layers' thickness as indicated by the simulation slightly differs from that obtained by ellipsometry in Figure S5(c). Hematite and ITO layer thicknesses of 32 and 269 nm, respectively, were used to simulate the front side spectrophotometry measurement presented in Figure 2(a) in the article, whereas the backside measurement (which was taken from a different sample position) presented in Figure 2(b) was fitted with thicknesses of 33 nm and 269.5 nm, respectively. The differences between the measured and the simulated absorptance spectra are used as a gauge for error estimation. For the incremental hematite absorptance in Equation (1) in the article, we used the thicknesses found for the front illumination because front and back EQE measurements were done on the same position of the sample, and the simulated reflectance and transmittance of the front illumination described the measurements

better. Hence, the reported thickness values for the sample in Figure S1(a) are 32 nm for hematite and 269 nm for ITO.

EQE and absorptance spectra

Figure S8 replots in the same graph the results presented in Figures 3a and 3b in the article.
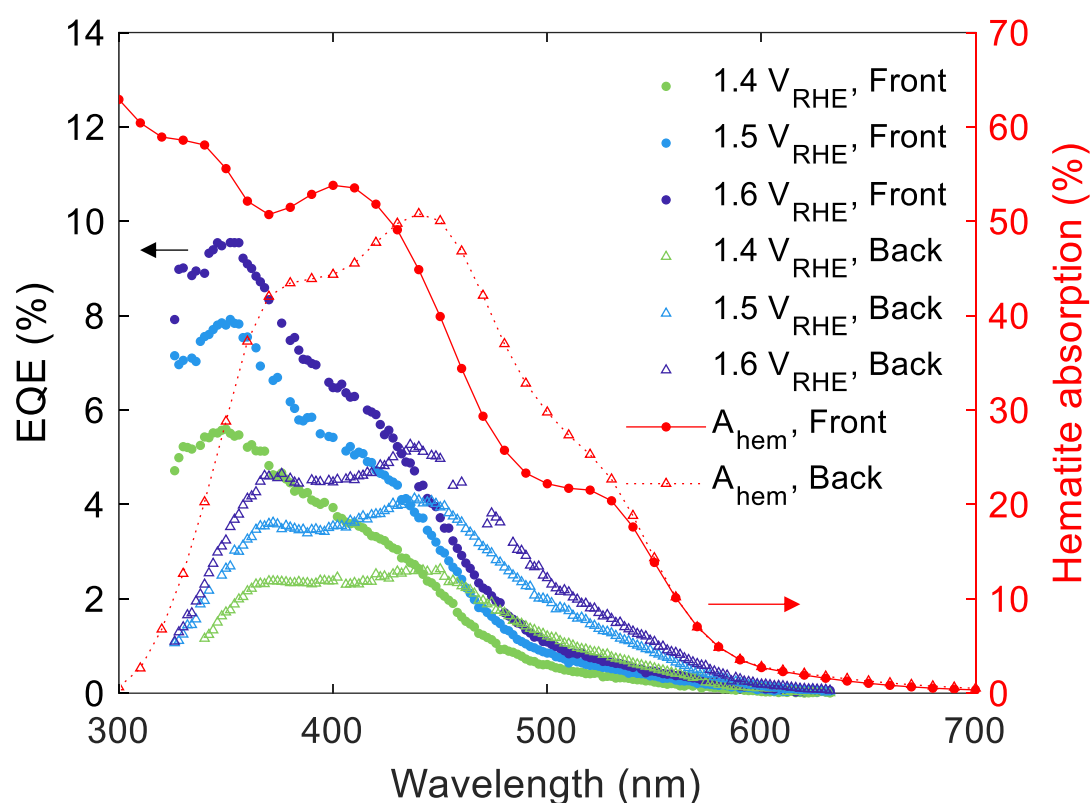

Figure S8. EQE and absorptance spectra of a 32 nm thick film hematite photoanode. EQE spectra measured at potentials of 1.4, 1.5 and 1.6 V_{RHE} (green, blue and purple curves, respectively) with front and back monochromatic probe light illuminations (full circles and empty triangles, respectively) riding a white-light bias in front of the PEC cell, overlaid with the calculated absorptance within the hematite layer (A_{hem}) for front and back illumination (full circles and empty triangles, respectively) in water at normal incidence (red curves, secondary y-axis on the right).
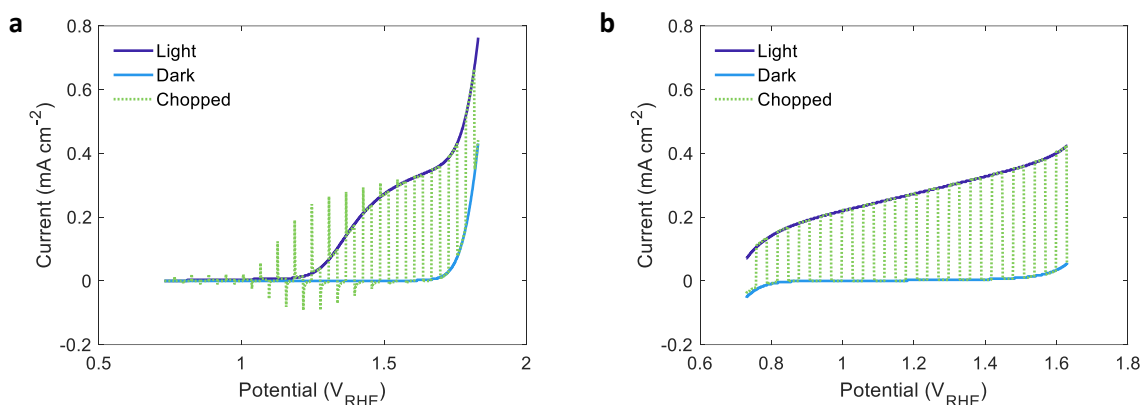
Photocurrent voltammograms

a

b

Figure S9. Photocurrent voltammograms of the thin (32 nm) film hematite photoanode from Figure S1(a). Linear sweep voltammograms measured in 1 M NaOH aqueous electrolyte without (a) and with (b) 0.5 M H_2O_2 hole scavenger in dark (solid light blue lines), under front continuous illumination (solid dark blue lines), and chopped illumination (dotted green lines) of a white-light LED (Mightex Systems, 6500K "glacial white" spectrum) calibrated to 100 mW/cm^2. The photocurrent presented in Figure 4(a) in the article was obtained by subtracting the dark measurement from the light one for both 1 M NaOH and 1 M NaOH + 0.5 M H_2O_2 aqueous electrolytes.
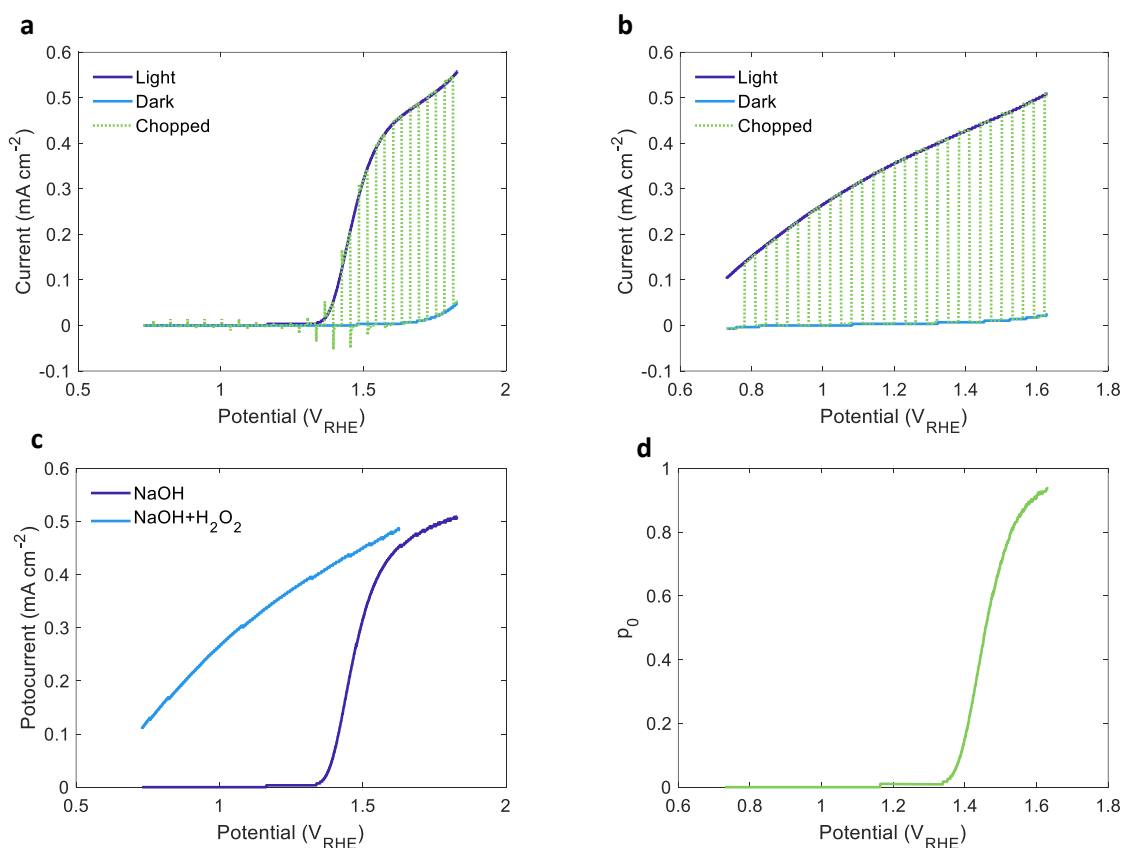
a

b

c

d

Figure S10. Photocurrent voltammograms of the ultrathin (7 nm) film hematite photoanode from Figure S1(b). Linear sweep voltammograms measured in 1 M NaOH aqueous electrolyte without (a) and with (b) 0.5 M H_2O_2 hole scavenger in dark (solid light blue lines), under front continuous illumination (solid dark blue lines) and front chopped illumination (dotted green lines) of a white-light LED (Mightex Systems, 6500K "glacial white" spectrum) calibrated to 100 mW/cm^2. The photocurrent presented in (c) was obtained by subtracting the dark measurement from the light one for both 1 M NaOH and 1 M NaOH + 0.5 M H_2O_2 aqueous electrolytes. (d) The charge carrier collection efficiency at the surface (p_0) obtained from the ratio between the photocurrents measured without and with H_2O_2.

Intensity modulated photocurrent spectroscopy (IMPS) measurements

The photocurrent in a photoelectrochemical cell is controlled by the applied potential and light intensity. There are three possibilities to measure the dynamic relations between these quantities by the following methods: photoelectrochemical impedance spectroscopy (PEIS), intensity-modulated photocurrent spectroscopy (IMPS) and intensity-modulated photovoltage spectroscopy (IMVS). The three methods are interrelated such that the results of any one of them can be calculated from the results of the other two methods.[5] In this study, we used PEIS and IMVS measurements at bias potentials of 1.4, 1.5 and 1.6 V_{RHE} and white-light intensities of 50 and 100 mW/cm^2 (obtained with a white-light 4300K LED, LSW-2, Zennium, Zahner Electrik) to extract the IMPS spectra presented in Figure S11. The measured data points (circles) were fitted (solid lines) to an equivalent circuit model as discussed elsewhere.[6] The model deviation from the measurements was typically <2% in 1M NaOH and <5% in 1 M NaOH + 0.5 M H_2O_2 electrolytes, as shown in Figures S11(e) and S11(f), respectively. Larger deviations were observed at ac frequencies above 3 kHz.
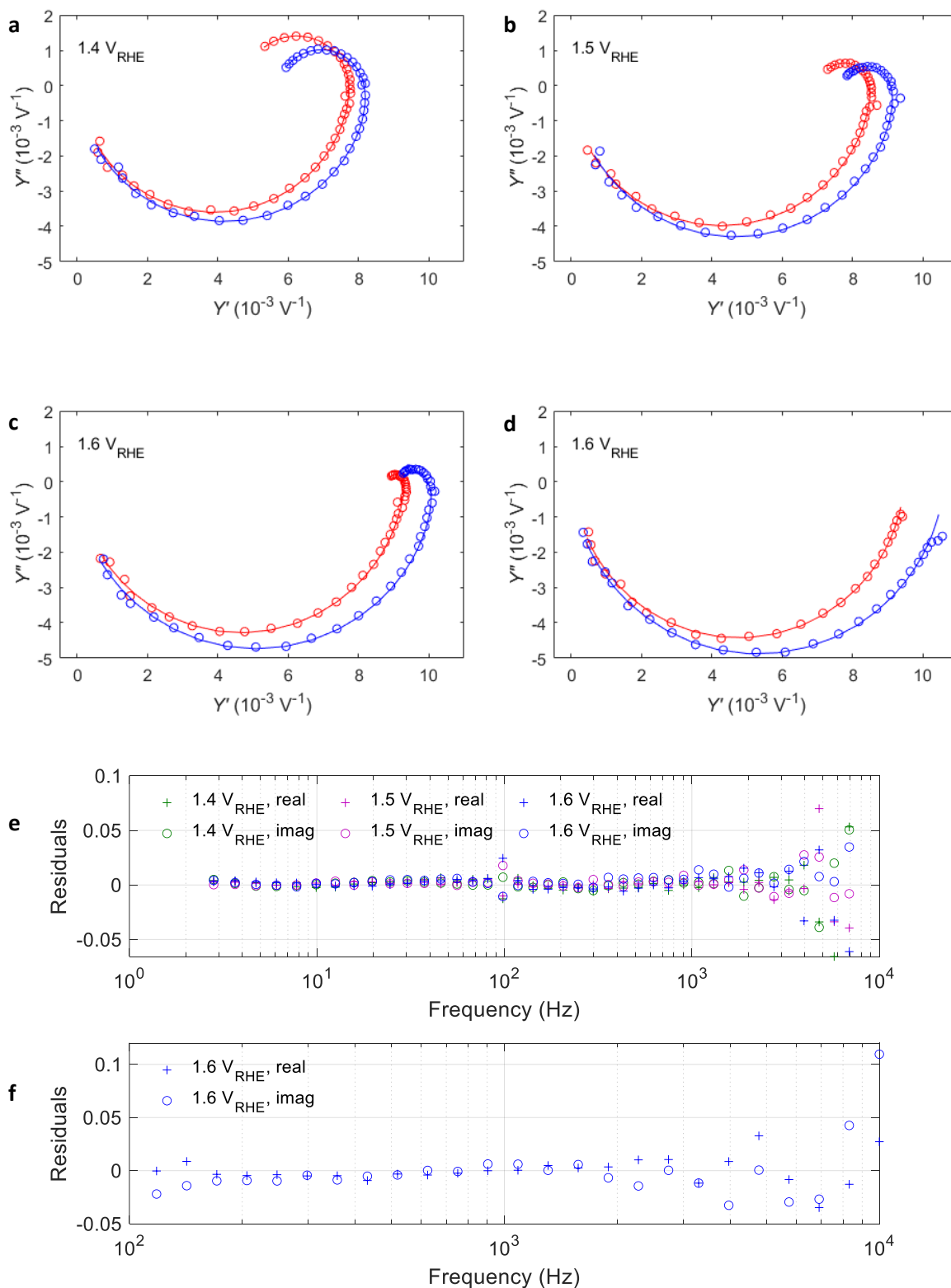
Figure S11. IMPS spectra of the thin (32 nm) film hematite photoanode. Measured (circles) and modeled (solid lines) IMPS spectra measured at potentials of 1.4 (a), 1.5 (b), and 1.6 V_{RHE} (c, d) under front illumination of a white-light LED at power densities of 50 (blue) and 100 mW/cm² (red), for measurements in 1M NaOH aqueous electrolytes without (a, b, c) and with 0.5 M H_2O_2 (d). (e, f) Depict the residuals for the real part (plus signs) and the imaginary part (circles) between measured and calculated results for 1.4 (green), 1.5 (purple), and 1.6 V_{RHE} (blue) in 1M NaOH electrolyte without (e) and with 0.5 M H_2O_2 (f).

Figure S12 compares the hole and surface recombination currents obtained from the IMPS analysis with linear sweep voltammograms measured with and without white light bias in the Zahner CIMPS system, indicating very good agreement which increases the confidence in our analysis.
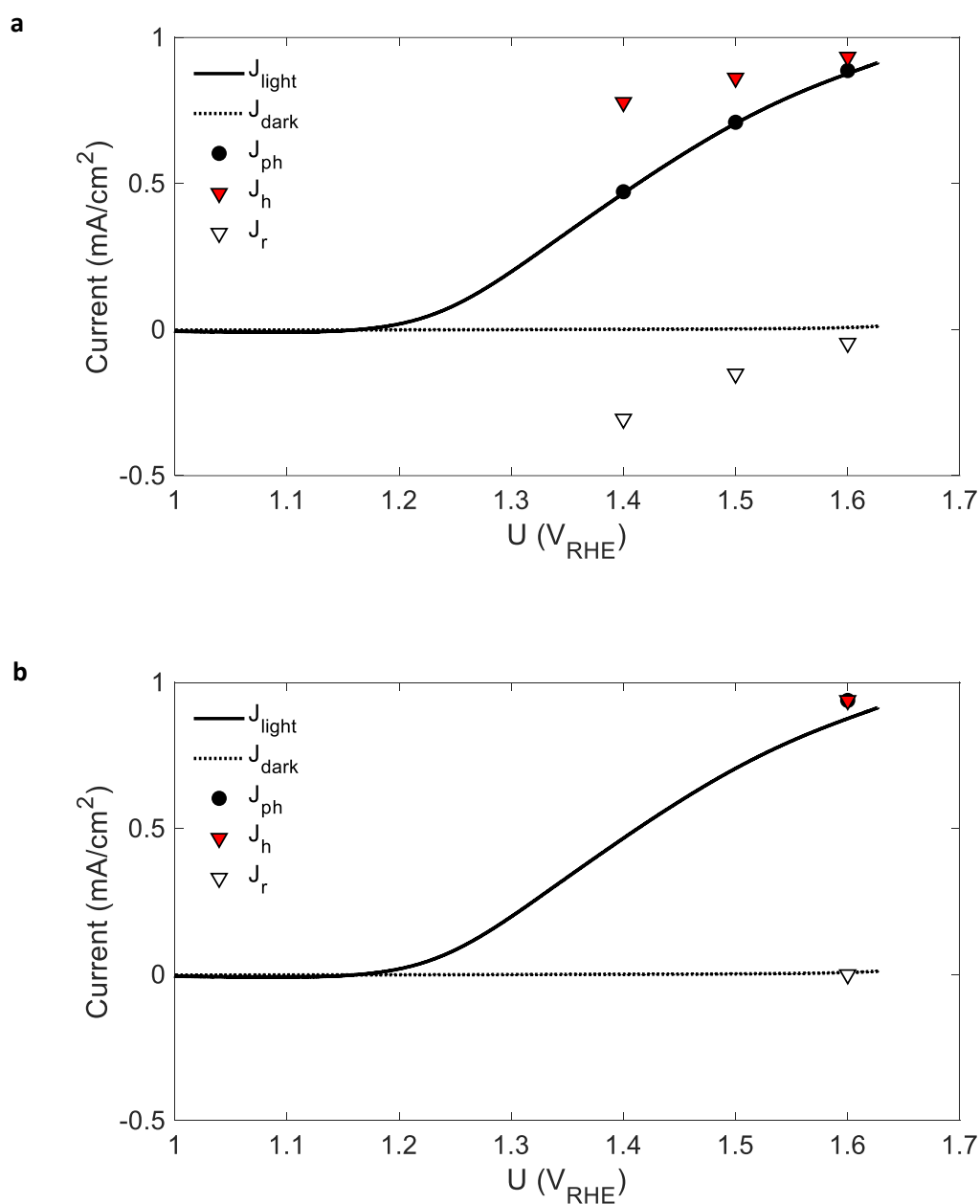
Figure S12. Comparison of IMPS results with photocurrent voltammetry measurements. J_h (hole current, red triangles), J_r (surface recombination current, white triangles) and J_{ph} (photocurrent, the sum of the hole and surface recombination currents, black circles) as a function of the applied potential, for the IMPS measurements presented in Figure S10 for the thin (32 nm) film hematite photoanode, measured in (a) 1M NaOH and (b) 1 M NaOH + 0.5 M H_2O_2 aqueous electrolytes. Solid and dashed lines represent linear sweep voltammograms measured with and without white light bias, respectively.

Table S1 summarizes the results presented in Figure S12, presenting the hole and surface recombination currents obtained without and with hole scavenger (H_2O_2) from the IMPS measurements presented in Figure S11. It also compares the ratio between the photocurrent and hole current (from Figure S12) to the charge transfer efficiency p_0 (at the same potentials) presented in Figure 4b in the article (based on the ratio between the photocurrent measured without and with H_2O_2). We note the different light sources used in these measurements, a 6500K white-light LED (Mightex Systems) in the voltammetry measurements and a 4300K white-light LED (LSW-2, Zennium, Zahner Electrik) in the IMPS measurements. Although the light intensity was calibrated to 100 mW/cm^2 in both cases, different emission spectra of these light sources (see Figure S14) may lead to different photocurrents. We use the p_0 results obtained from voltammetry measurements with and without H_2O_2 in the extraction of the photogeneration yield spectrum and spatial charge carrier collection efficiency profiles because these measurements were carried out with the same light source as the EQE measurements.

Table S1. IMPS results. The hole (J_h) and surface recombination (J_r) currents measured in 1M NaOH and 1M NaOH + 0.5M H_2O_2 aqueous electrolytes obtained from the analysis presented in Figure S12 of the IMPS spectra presented in Figure S11. The rightmost columns present the ratio between the photocurrent ($J_{photo} = J_h + J_r$) and the hole current (J_h), and the charge transfer efficiency values (p_0) from Figure 4(b) in the article.

	Potential (V_{RHE})	J_h (mA/cm^2)	J_r (mA/cm^2)	$\dfrac{J_{photo}}{J_h}$	p_0
	1.4	0.30	-0.12	0.61	0.57
NaOH	**1.5**	0.33	-0.06	0.82	0.79
	1.6	0.36	-0.02	0.95	0.88
H₂O₂	**1.6**	0.36	0	1	N/A

EQE integration

Figure S13 overlays the integrated photocurrent values (open circles) obtained from the EQE spectra presented in Figure 3 in the article on the photocurrent voltammograms (solid lines) presented in Figure 4 in the article. The front and back illumination results are presented in blue and green, respectively. The match between the integrated values and the directly measured results is excellent for front illumination (blue), and good for back illumination (green). In the latter case, the integrated values are lower by ~10% than the photocurrent voltammogram because the latter was measured while the photoanode was positioned slightly closer to the white-light LED in back illumination.

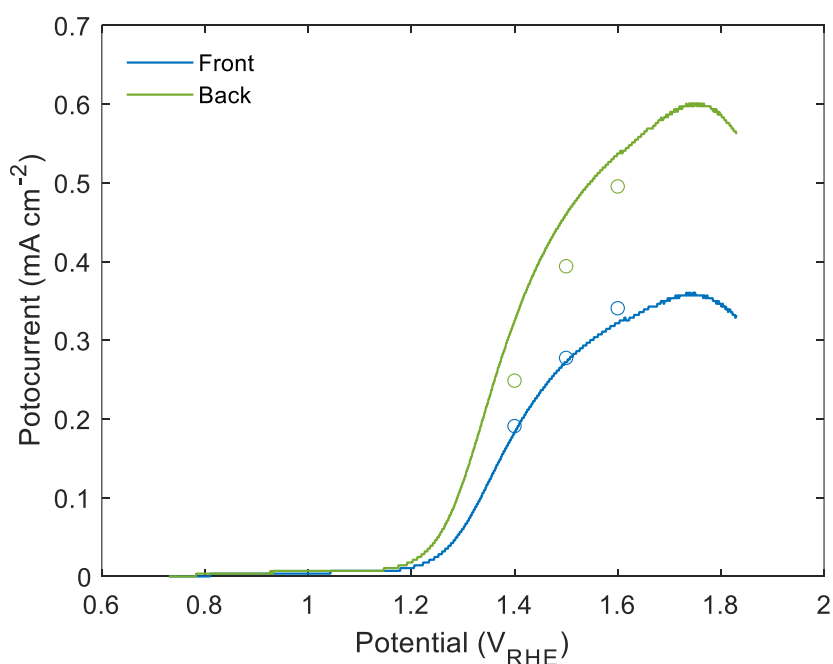**Figure S13. Integrated EQE results vs. direct photocurrent measurements.** Integrated photocurrent values (open circles) obtained from the EQE spectra presented in Figure 3 in the article for front (blue) and back (green) EQE measurements, overlaid with the photocurrent voltammogram (solid lines) presented in Figure 4 in the article. Both measurements were carried out in 1M NaOH aqueous electrolytes.

LED spectra

Figure S14 presents the spectrum of the white-light LED used for the EQE and voltammetry measurements (6500K white LED, Mightex Systems); the spectrum of the white-light LED used for the IMPS measurements (4300K white LED, LSW-2, Zennium, Zahner Electrik); and the standard AM1.5G spectrum.[7] We calculated, for the presented wavelength range (300-900 nm), integrated light intensities of 68 and 65 mW/cm^2 for the AM1.5G spectrum and the lamp used for the EQE measurements, respectively. The lamp used for the IMPS measurements was measured 7.9 cm further away from the photoanode position to avoid the setup shadowing on the detector, and therefore its integrated intensity was only 40 mW/cm^2. To enable easy comparison between the light spectra at the photoanode position, this spectrum was multiplied by a fixed ratio of 68/40 and plotted on the same axis.
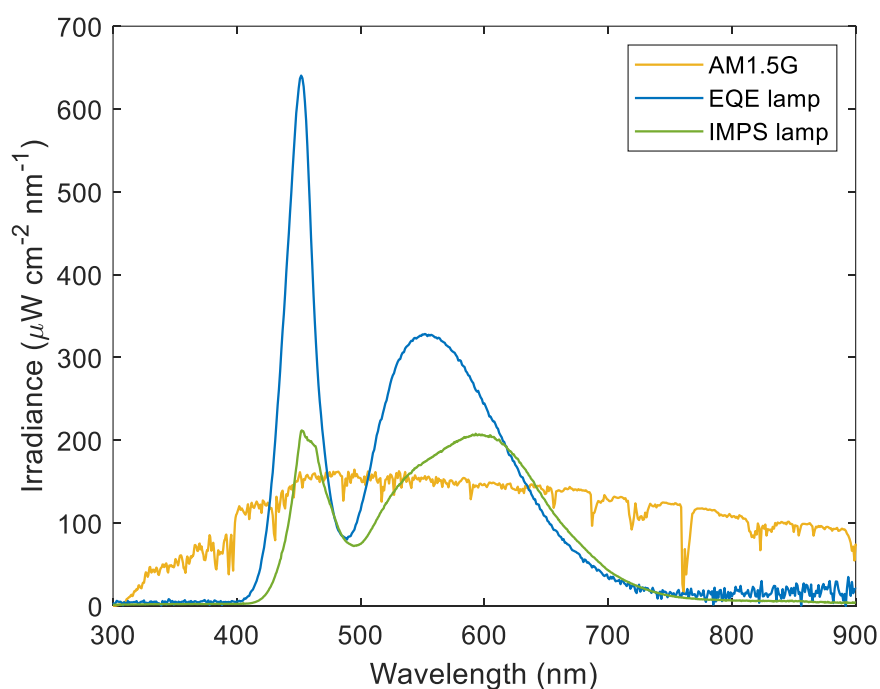

Figure S14. LED light intensity spectra. The measured intensity of the high-power white-light LED used for the EQE and voltammetry measurements (blue), the white-light LED used for the IMPS measurements (green) and the standard AM1.5G spectrum converted to the same units.

Mott-Schottky analysis

The analysis of the Mott-Schottky plots of the thin (32 nm) film hematite photoanode presented in Figure 4(c) in the article was done as follows. Considering an equivalent circuit in which the Helmholtz layer capacitance (C_H) is connected in series with two parallel capacitors describing the space charge layer capacitance (C_{SCR}) and the semiconductor surface states capacitance (C_{SS}), and assuming C_{SS} is negligible compared to C_{SCR} and that C_H is much greater than C_{SCR}, *i.e.* the potential drop falls mainly on the space charge region, the majority charge carrier concentration (n_0) can be calculated using the Mott-Schottky formula:[8]

$$\frac{1}{C^2} = \frac{2}{n_0 q \varepsilon_r \varepsilon_0 A^2}[U_{fb} + U] + \frac{1}{C_H^2} \qquad \text{(Equation S1)}$$

where ε_r = 33 is the relative dielectric constant of hematite,[9] ε_0 is the vacuum permittivity, q is the elementary charge, A is the nominal (projected) area of the photoanode exposed to the electrolyte (0.283 cm² in our cappuccino cell), U is the applied potential and U_{fb} is the flat-band potential. Using the results presented in Figure 4(c) of the article, the majority (electron) charge carrier concentration (n_0) was found to be $(3.60 \pm 0.05) \times 10^{19}$ cm^{-3}, and the flat-band potential (U_{fb}) was found to be 0.40 ± 0.02 V$_{RHE}$. The errors were calculated based on the errors in the slopes and intercepts computed by linear regression of the capacitance – potential measurements at different frequencies, and are presented in Table S2. From these values, the width of the space charge region (W_{SCR}) was extracted using the following formula:[10]

$$W_{SCR} = \sqrt{\frac{2\varepsilon_r \varepsilon_0}{q n_0}(U - U_{fb})} \qquad \text{(Equation S2)}$$

The W_{SCR} values obtained for the different frequencies are presented in Table S3. The errors were calculated based on the measurement errors in n_0 and U_{fb}, stimated by averaging the standard deviation (stdev, σ) values obtained for the different frequencies presented in Table S2.

Table S2. Mott-Schottky analysis error calculation.

Frequency (Hz)	5010	6310	7940
Intercept mean (10^{11} F^{-2} V)	-1.80	-1.70	-1.70
Intercept stdev (10^{11} F^{-2} V)	0.06	0.08	0.09
Slope mean (10^{11} F^{-2}V^{-1})	4.24	4.18	4.19
Slope stdev (10^{11} F^{-2}V^{-1})	0.05	0.06	0.07
n_0 mean (10^{19} cm^{-3})	3.57	3.62	3.61
n_0 stdev (10^{19} cm^{-3})	0.04	0.05	0.06
U_{fb} mean (V)	0.41	0.40	0.40
U_{fb} stdev (V)	0.01	0.02	0.02

Table S3. The space charge region width obtained for different applied potentials, calculated using Equation S2. The space charge region widths found for the potentials applied in the EQE measurements are bolded. The stdev was found to be 0.1 nm in all cases.

Potential (V_{RHE})	W_{SCR} (nm)
0.9	7.1
1	7.8
1.1	8.4
1.2	9.0
1.3	9.5
1.4	**10.1**
1.5	**10.5**
1.6	**11.0**

Finding the relevant range of $\bar{p}$

The lowest possible value of $\bar{p}$ was found to be 0.1 because lower values result in $\xi(\lambda)>1$, which is not physical. Figure S15(a) presents the initial guess spectrum, $\xi_{0.1}^0(\lambda)$, found by solving Equation (2) in the article using $\bar{p} = 0.1$ and its six corrected spectra using the different measurement datasets and Equation (4) in the article. The error bars represent the calculation error as estimated based on the difference between the measured and calculated optical absorptance (see Error Analysis section). Figure S15(b) compares the initial guess spectrum, $\xi_{0.1}^0(\lambda)$, with the respective corrected solution, $\xi_{0.1}^1(\lambda)$, which is defined as the mean spectrum of the respective $\xi_{0.1}^{corrected}(\lambda)$ sixfold spectra, as defined by Equation 4 in the article. The error bars represent the standard deviation of the six corrected spectra. The measured EQE spectra (from Figure 3 in the article) are compared in Figures S15(c) and S15(d) (for front and back EQE, respectively) with the calculated EQE spectra obtained using the $\xi_{0.1}^1(\lambda)$ spectrum (for $\bar{p} = 0.1$), assuming that the spatial collection efficiency profile decreases with depth (x) according to the single exponential decay function expressed in Equation (3) in the article, where p_0 is fixed by the hole scavenger photocurrent voltammetry measurements presented in Figure 4(b) in the article. We used the same p_0 values for both front and back illuminations since in both cases the white light bias source (LED), which had 2-3 orders of magnitude higher intensity than the monochromatic probe light, was positioned in front of the sample. Hence, both cases shared the same spatial collection efficiency profile. The agreement between the measured and calculated EQE spectra is reasonable.
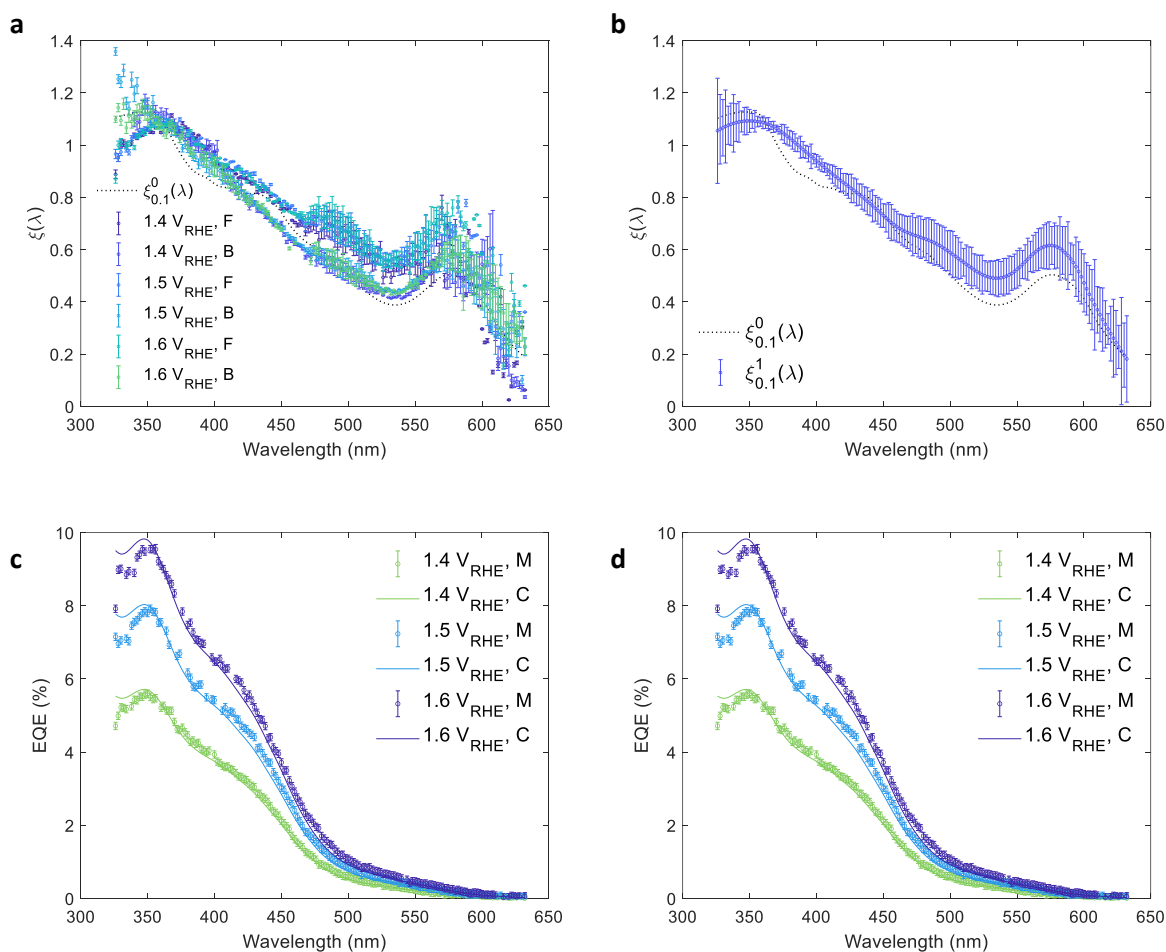
Figure S15. Finding the minimal $\bar{p}$ value. (a) The initial guess spectrum $\xi_{0.1}^0(\lambda)$ (dotted black curve) obtained by solving Equation (2) in the article for $\bar{p}=0.1$, and its sixfold corrected spectra $\xi_{0.1}^{corrected}(\lambda)$ defined in Equation (4) in the article (other colors). F and B stand for front and back illuminations. (b) Comparison of the initial guess spectrum $\xi_{0.1}^0(\lambda)$ (dotted black line) to the averaged corrected $\xi_{0.1}^1(\lambda)$ spectrum and standard deviation values (blue). (c) and (d) Comparison between the measured (M) and the calculated (C) EQE spectra at different potentials as indicated in the legend, for front (c) and back illuminations (d). The calculated EQE spectra were obtained using the average corrected $\xi_{0.1}^1(\lambda)$ spectrum (for $\bar{p}=0.1$) and assuming the spatial collection efficiency profile described in Equation (3) in the article.

The highest possible value of $\bar{p}$ was found to be 0.3 because higher values result in worse fitting of the measured EQE as well as worse agreement between the different corrected spectra of $\xi_{0.3}^0(\lambda)$. Figure S16(a) presents the initial guess spectrum $\xi_{0.3}^0(\lambda)$ found by solving Equation (2) in the article using $\bar{p}=0.3$ and its six corrected spectra using the different measurement datasets and Equation (4) in the article. The error bars represent the calculation error as estimated based on the difference between the measured and calculated optical absorptance (see Error

Analysis section). Figure S16(b) compares the initial guess spectrum $\xi_{0.3}^0(\lambda)$ with the respective averaged corrected solution $\xi_{0.3}^1(\lambda)$ which is defined as the mean spectrum of the respective $\xi_{0.3}^{corrected}(\lambda)$ sixfold spectra, as defined by Equation 4 in the article. The error bars represent the standard deviation of the six corrected spectra. The measured EQE spectra (from Figure 3 in the article) are compared in Figure S15(c) and Figure S16(d) (for front and back EQE, respectively) with the calculated EQE spectra obtained using the $\xi_{0.3}^1(\lambda)$ spectrum (for $\bar{p} = 0.3$), assuming that the spatial collection efficiency profile decreases with depth (x) according to the single exponential decay function expressed in Equation (3) in the article, where p_0 is fixed by the hole scavenger measurements presented in Figure 4(b) in the article. We used the same p_0 values for both front and back illuminations since in both cases the white light bias source (LED), which had 2-3 orders of magnitude higher intensity than the monochromatic probe light, was positioned in front of the sample. Hence, both cases shared the same spatial collection efficiency profile. These figures show worse agreement than in Figure S15. The disagreement was found to worsen with higher $\bar{p}$ values. Therefore, we concluded that the upper limit of $\bar{p}$ should be 0.3.
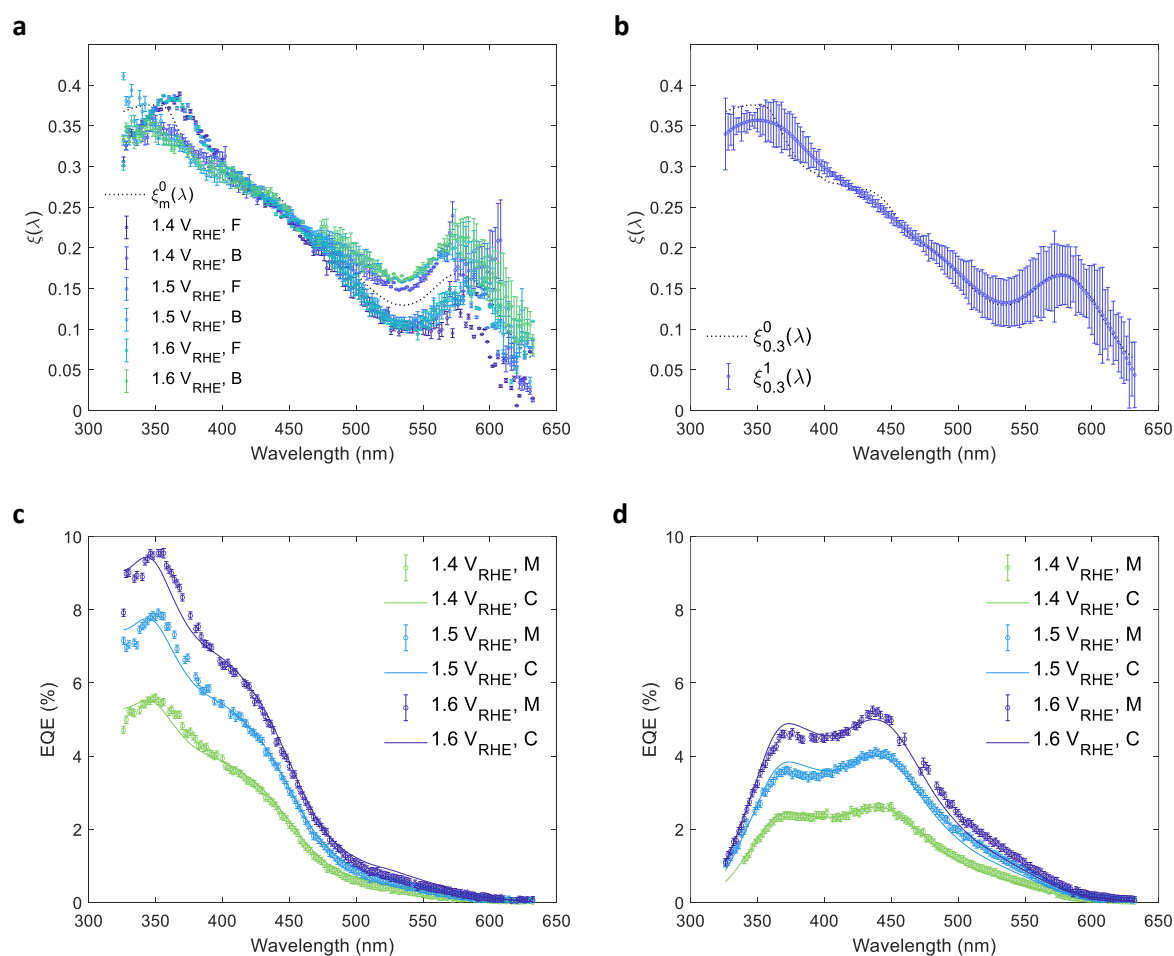
Figure S16. Finding the maximal $\bar{p}$ value. (a) The initial guess spectrum $\xi_{0.3}^0(\lambda)$ (dotted black curve) obtained by solving Equation (2) in the article for $\bar{p} = 0.3$, and its sixfold corrected spectra $\xi_{0.3}^{corrected}(\lambda)$ defined in Equation (4) in the article (other colors). F and B stand for front and back illuminations. (b) Comparison of the initial guess spectrum $\xi_{0.3}^0(\lambda)$ (dotted black line) to the averaged corrected $\xi_{0.3}^1(\lambda)$ spectrum and standard deviation values (blue). (c) and (d) Comparison between the measured (M) and the calculated (C) EQE spectra at different potentials as indicated in the legend, for front (c) and back illuminations (d). The calculated EQE spectra were obtained using the average corrected $\xi_{0.3}^1(\lambda)$ spectrum (for $\bar{p} = 0.3$) and assuming the spatial collection efficiency profile described in Equation (3) in the article.

Extracting $\xi(\lambda)$ of the 32 nm hematite photoanode

Figure S17 presents, by taking $\bar{p}_6 = 0.15$ as an example, the agreement between the measured and calculated EQE spectra. It demonstrates improved agreement obtained by substituting $\xi_{0.15}^0(\lambda)$ used for solving Equation (1) in the article in the first iteration with $\xi_{0.15}^1(\lambda)$ used for solving it in the second iteration, using the $p(x)$ function expressed in Equation (3) in the article.
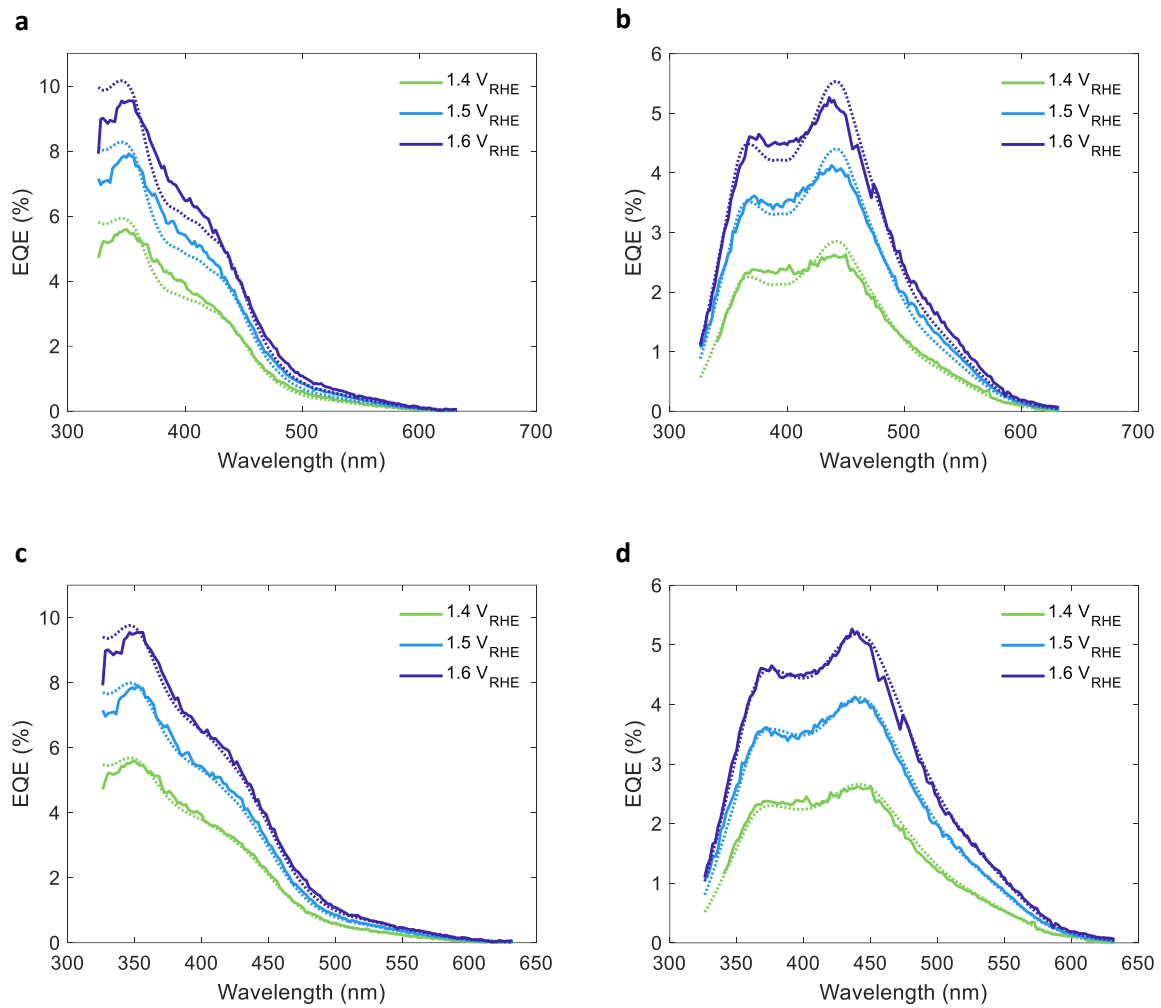
Figure S17. Comparison of EQE agreement obtained in iterations #1 and #2 (example). Comparison between the measured (solid lines) and the calculated (dotted lines) EQE spectra at different potentials as indicated in the legend, for front (a and c) and back (b and d) illuminations. The calculated EQE spectra were obtained using the $\xi_{0.15}^0(\lambda)$ spectrum (for $\bar{p} = 0.15$) in the first iteration (a and b) and the $\xi_{0.15}^1$ spectrum in the second iteration (c and d) and assuming the spatial collection efficiency profile described in Equation (3) in the article.

Figure S18 presents the minority charge carrier collection length (ℓ) values obtained by solving Equation (1) in the article with the initial guess spectra, $\xi_{\bar{p}_m}^0(\lambda)$, in the first iteration, and with the selected averaged spectra, $\xi_{\bar{p}_m}^1(\lambda)$, in the second iteration, using the spatial collection efficiency profile presented in Equation (3) in the article. The markers and the error bars represent, respectively, the mean value and the standard deviation (σ) of the ℓ values obtained for the six EQE datasets (three potentials, two illumination directions), for each $\bar{p}_m$ selection. The mean carrier collection length values agree within ~3σ, indicating that the $\xi_{\bar{p}_m}^0(\lambda)$ spectra

obtained by solving Equation (2) in the article serve well as initial guesses. The mean value of the error in the second iteration was 56% of the error in the first iteration, indicating improved precision in the second iteration.
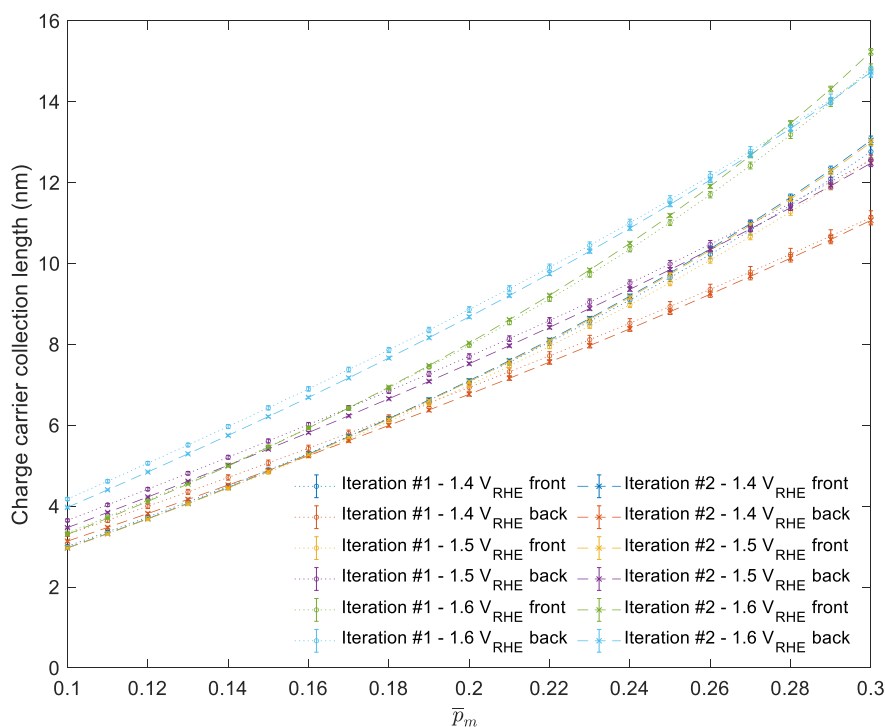

Figure S18. Comparison of ℓ values obtained in the first and second iterations. The mean and standard deviation values of the carrier collection length (ℓ) obtained in the first and second iterations.

Figure S19 presents the initial guess spectra $\xi^0_{\bar{p}_m}(\lambda)$ calculated using Equation (2) in the article for $\bar{p}$ values between 0.15 and 0.2, and their corrected spectra using the sixfold measurement datasets (three potentials and two illumination directions). These values were selected because they yielded minimal variations for datasets obtained at different potentials and illumination directions, as shown in Figure 5(a) in the article. The error bars represent the calculation error as estimated based on the difference between the measured and calculated optical absorptance (see Error Analysis section). This figure shows clearly the better agreement obtained between the different corrected spectra compared to Figure S15(a) and Figure S16(b),

indicating that the $\xi(\lambda)$ spectrum is independent on the potential and probe illumination direction, as expected.
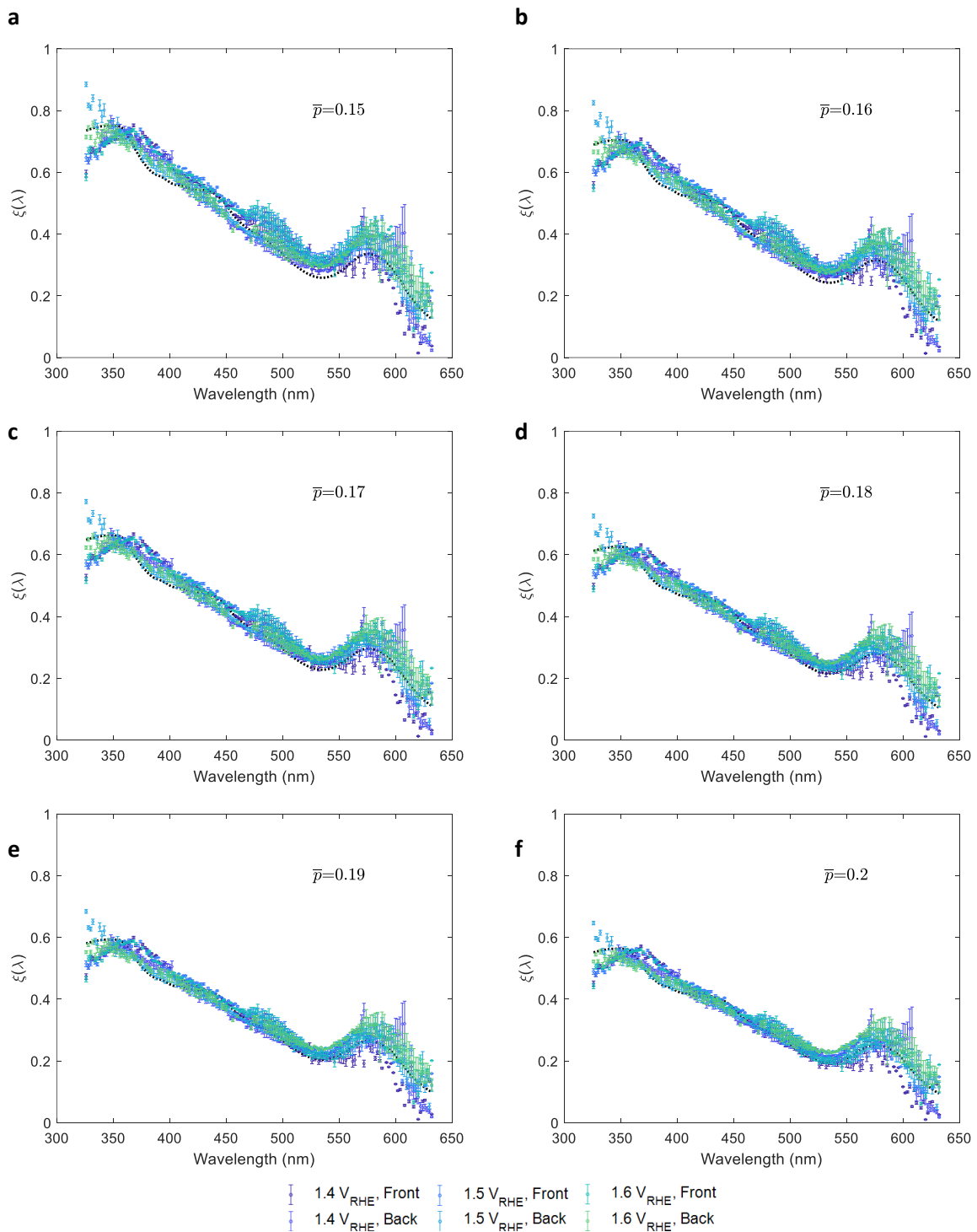

Figure S19. The agreement between the $\xi_{\overline{p}_m}^{corrected}(\lambda)$ sixfold spectra of the chosen initial guesses. The initial guess spectra $\xi_{\overline{p}_m}^0(\lambda)$ (black dotted line) calculated using Equation (2) for $\overline{p}$ values of 0.15 (a), 0.16 (b), 0.17 (c), 0.18 (d), 0.19 (e) and 0.2 (f), and their corrected spectra using the sixfold measurement datasets (other colors).

Extracting $\xi(\lambda)$ of the 7 nm hematite photoanode

The photogeneration yield of the ultrathin (7 nm) film hematite photoanode was found similarly to that of the thin (32 nm) film hematite photoanode, using the algorithm presented in Figure 1 of the article. Photocurrent voltammetry measurements with and without hole scavenger (H_2O_2) were used to extract the charge transfer efficiency at the surface, p_0 (see Figure S10). To generate the $\xi^0_{\bar{p}_m}(\lambda)$ initial guesses, we used nine $\bar{p}$ values between 0.92 and 1 with 0.01 increments. This range was selected since lower values resulted with poor agreement between the measured and the calculated EQE, as seen in Figure S20(a) and S20(b). The measurement error could not be calculated due to lack of data in the early measurement files, so it was estimated as 0.1% of the EQE. Since this photoanode was measured at only one potential for both front and back illuminations, the wavelength-dependent normalized standard deviation ($\overline{(\sigma_{\bar{p}_m}(\lambda)/\xi^1_{\bar{p}_m}(\lambda))}$) of the twofold corrected spectra did not suffice to indicate the physical solutions. Therefore, both criteria, the wavelength-dependent relative standard deviation from the first iteration (presented in Figure S20(c)) and the variance between the measured and calculated EQE spectra from the second iteration (presented in Figure S20(d)), were considered. The minimal variation according to both criteria corresponded to the last two $\bar{p}_m$ initial guess values (0.99 and 1). Their respective $\xi^1_{\bar{p}_m}(\lambda)$ solutions, which overlapped, were averaged and presented as the $\xi(\lambda)$ spectrum of the ultrathin (7 nm) film hematite photoanode in Figure 5 in the article.
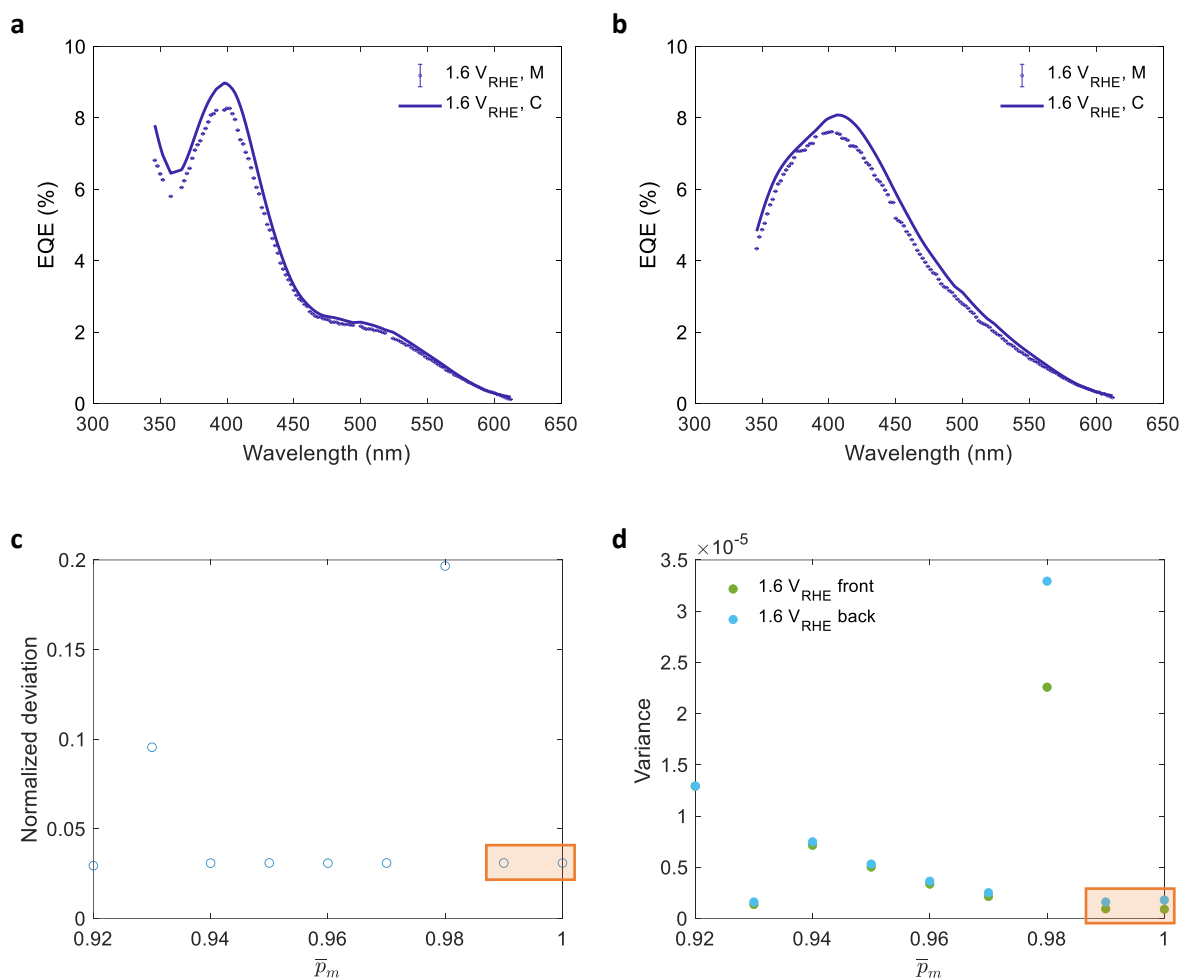
Figure S20. The $\bar{p}$ range selected for extracting the photogeneration yield spectrum, $\xi(\lambda)$, of a 7 nm thick film hematite photoanode. (a) and (b) Comparison between the measured (M) and the calculated (C) EQE spectra for front and back illuminations, respectively. The calculated EQE spectra were obtained using the $\xi^1_{0.92}(\lambda)$ spectrum (for $\bar{p} = 0.92$) and assuming the spatial collection efficiency profile described in Equation (3) in the article. (c) The wavelength-averaged normalized deviation of the twofold $\xi^{corrected}_{\bar{p}_m}(\lambda)$ spectra vs the respective $\bar{p}_m$ initial guess values. (d) The wavelength-averaged variance between EQE spectra measured for front (green) and back (cyan) illuminations and the corresponding calculated EQE spectra obtained for different initial guesses ($\bar{p}_m$). The circles corresponding to $\bar{p}_m$=0.92 overlap each other, and therefore only one circle is seen. The lowest two points in both (c) and (d) (framed by the orange box) were selected as the "best" solutions.

Since nearly the same $\xi^1_{\bar{p}_m}(\lambda)$ solution was found for both selected $\bar{p}_m$ values, the corresponding collection length values found assuming the simplified $p(x)$ function from Equation (3) in the article were almost identical. The interim spatial collection efficiency profiles ($p(x)$) obtained in the first and second iteration for the ultrathin (7 nm) film photoanode revealed approximately constant behaviour, since all charge carrier collection length values found were considerably larger than the hematite

layer thickness ($\ell >> d$). Therefore, the simplified $p(x)$ function from Equation (3) was used for the third iteration and was not replaced by Equation (5).

Figure S21(a) presents the spatial collection efficiency profile ($p(x)$) obtained using the photogeneration yield presented in Figure 5(b) in the article (green line) and assuming the simplified $p(x)$ function from Equation (3) for front and back illuminations. Unlike for the 32 nm thick film photoanode, the spatial collection efficiency profile obtained for the ultrathin (7 nm) film photoanode is nearly constant across the entire film thickness. This is like the flat bands in nanocrystalline semiconductors with grains smaller than twice the Debye length.[13] The $p(x)$ obtained uncovers spatial collection efficiency of ~90% throughout the 7 nm hematite layer, demonstrating that the photocurrent is not limited by fast charge carrier recombination, but rather by the photogeneration yield which varies from 43% to 20% over the wavelength range. The agreement between the measured and calculated EQE spectra using the extracted $\xi(\lambda)$ spectrum is presented in Figure S21(b) and S21 (c) for front and back illuminations, respectively.
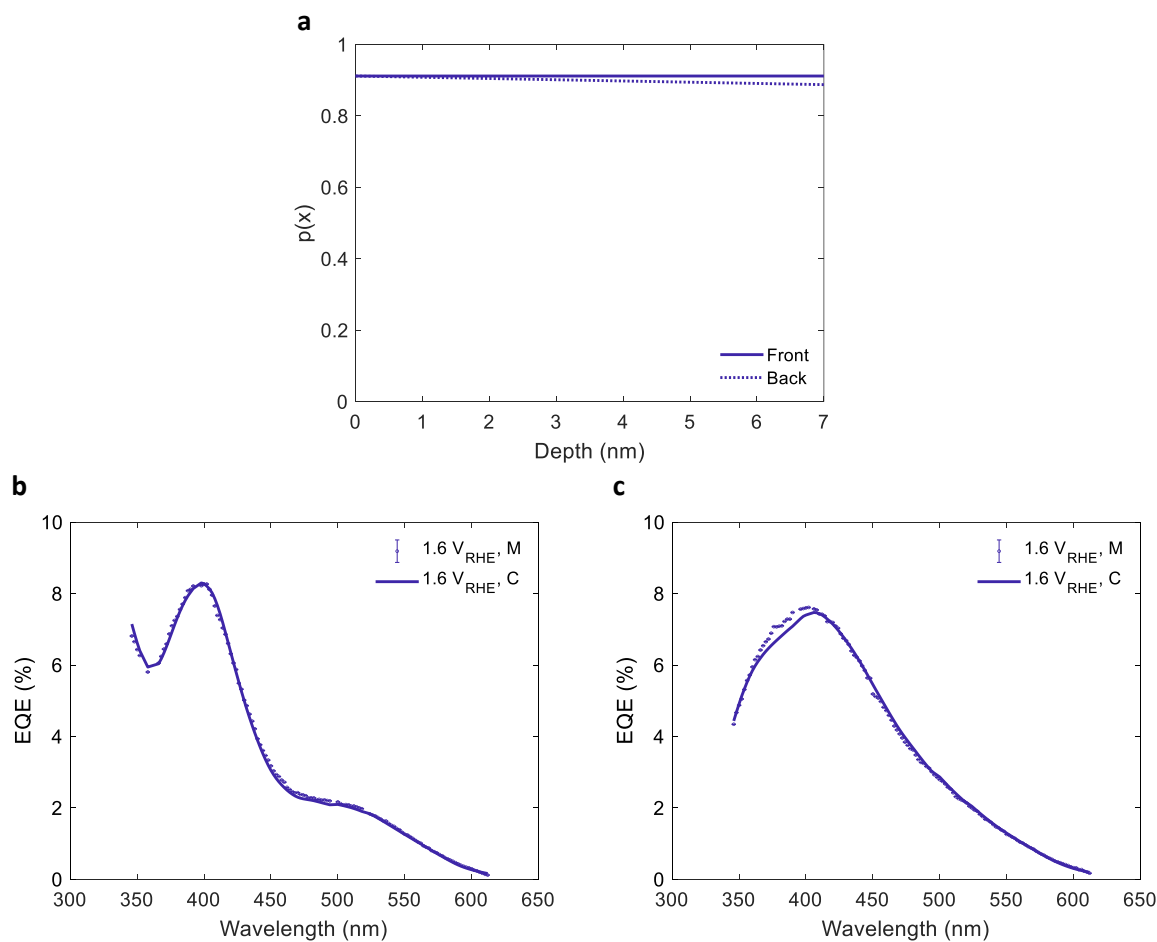
Figure S21. **The charge carrier collection efficiency profile, $p(x)$, of a 7 nm thick film hematite photoanode**. (a) The charge carrier collection efficiency profiles, $p(x)$, extracted in the third iteration, for EQE measured at front (solid line) and back illuminations (dotted line). (b,c) The agreement between the measured (M) and the calculated (C) EQE spectra for front (a) and back (b) illuminations assuming single exponential decay profile (as in Equation (3) in the article) and the $\xi(\lambda)$ spectrum of the ultrathin (7 nm) film hematite photoanode presented in Figure 5 in the article.

Fitting EQE assuming a uniform segment for the spatial collection efficiency

Figure S22 shows the spatial charge carrier collection efficiency profiles for the sixfold datasets (three potentials and two illumination directions) found to best fit the measured EQE spectra by solving Equation (1) in the article using the $\xi(\lambda)$ spectrum found in the first and second iterations and assuming the spatial collection efficiency profile is described by a single exponent as expressed in Equation (3) in the article. Figure S22(b) and S22(c) show the agreement between the calculated and measured EQE spectra for front and back illuminations, respectively. The

effective carrier collection length ℓ extracted for the different datasets increases with increasing potential, as summarized in Table S4.
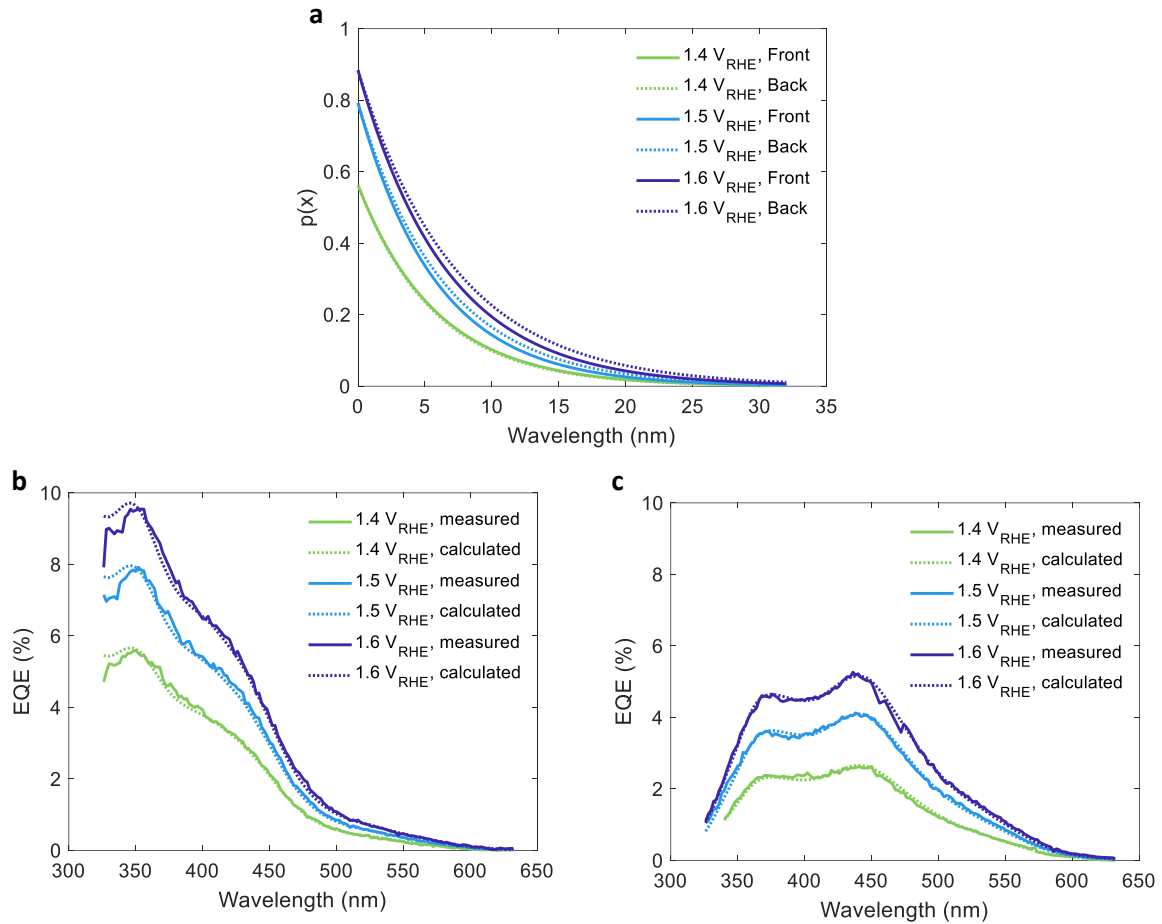

Figure S22. Fitting the EQE spectra with a single segment spatial collection efficiency profile. (a) The extracted spatial collection efficiency assuming single exponential decay profile (as in Equation (3) in the article). (b, c) The agreement between the measured (solid curves) and calculated (dotted lines) EQE spectra for front (b) and back (c) illuminations.

Table S4. The spatial collection efficiency decay constants fitted for a single segment $p(x)$ function

Potential (V_RHE)	ℓ (nm)	
	Front	**Back**
1.4	5.9 ± 0.1	5.7 ± 0.1
1.5	5.9 ± 0.1	6.4 ± 0.1
1.6	6.6 ± 0.1	7.3 ± 0.1

Table S5 compares the variance between the measured and calculated EQE spectra obtained by solving Equation (1) and assuming single- or two-segment $p(x)$ functions (Equations (3) and (5) in the article, respectively). The varaince was calculated by $\sum \frac{(EQE_{measured}\text{-}EQE_{calculated})^2}{N}$, where N is the number of the EQE measurement points (measured wavelengths). The standard deviation is the square root of the varaience and given in units of (%). The sum values show that the agreement for the two-segment $p(x)$ model is slightly better than for the single-segment model.

Table S5. The varaince between the measured and calculated EQE spectra using single- or two-segment $p(x)$ functions.

	1-segment $p(x)$ function according to Eq. (3)	2-segment $p(x)$ function according to Eq. (5)
1.4 V$_{RHE}$ - front	0.11	0.11
1.4 V$_{RHE}$ - back	0.06	0.04
1.5 V$_{RHE}$ - front	0.16	0.15
1.5 V$_{RHE}$ - back	0.08	0.08
1.6 V$_{RHE}$ - front	0.19	0.18
1.6 V$_{RHE}$ - back	0.07	0.08
Sum	0.68	0.64

Resolving the optical transitions

Four out of the five non-contributing Gaussians we resolved in the main manuscript (Figure 8) are consistent with the absorption peaks resolved in a study by Marusak *et al*[11] within a margin of 0.1 eV, as presented in Table S6.

Table S6. Peak energies of the resolved contributing and non-contributing optical transitions presented in Figure 8. The right column presents peak energies extracted from Figure 1 in reference 11.

Contributing excitations	Non-contributing excitations	Marusak *et al.* (Ref [11])
	2.0 eV	2.1 eV
2.4 eV	2.4 eV	2.3 eV
	2.5 eV	2.5 eV
3.0 eV	3.0 eV	3.0 eV
3.5 eV	3.6 eV	3.3 eV
		3.9 eV
4.8 eV (fixed)	4.8 eV (fixed)	4.8 eV

Figure S23 demonstrates that resolving the non-contributing component of the absorption coefficient spectrum into six Gaussian oscillators does not depend on the initial guess used, since the center energies found using two different initial guesses are the same (within a margin of 0.1 eV).
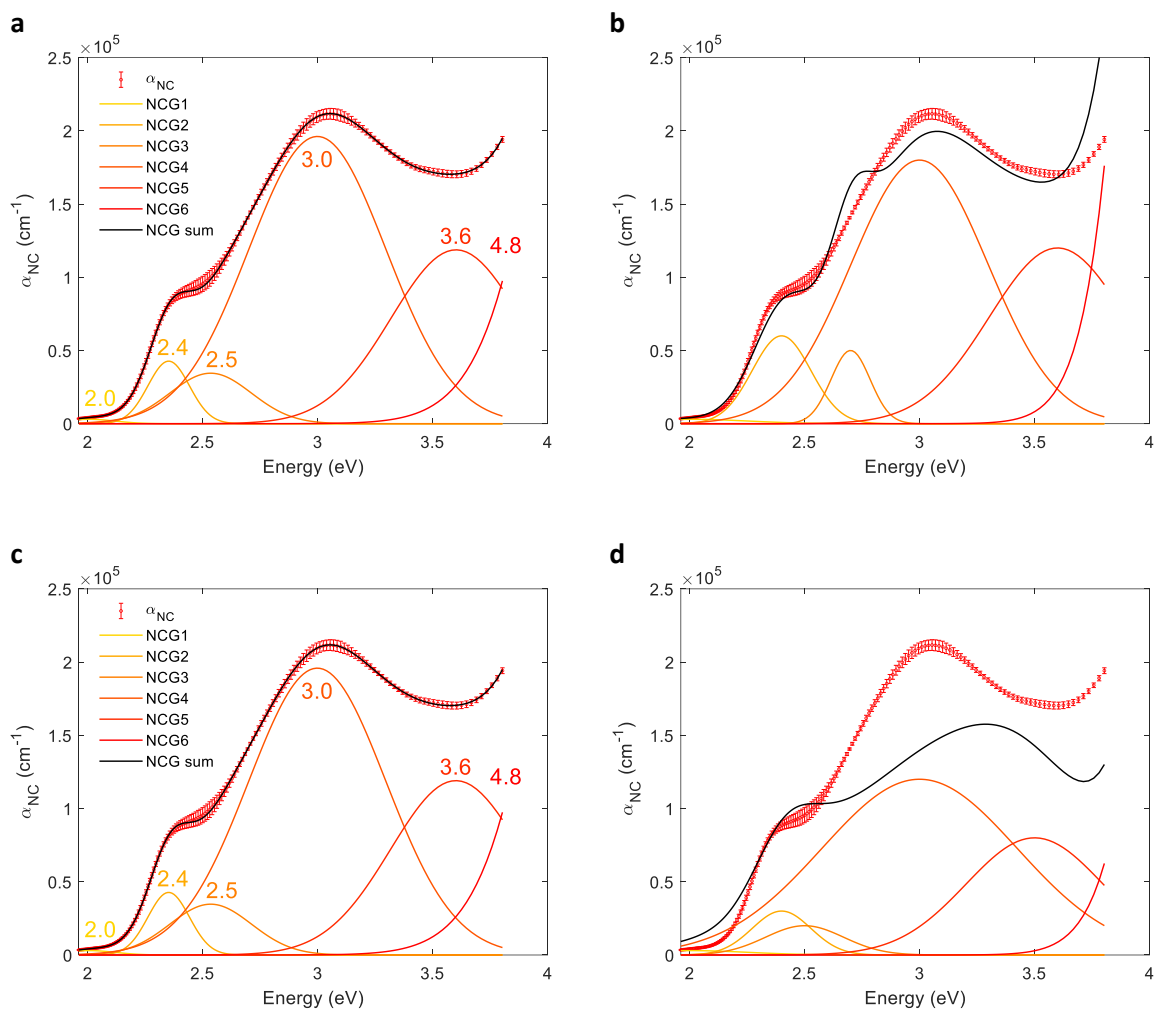
Figure S23. Resolving the non-contributing component of the absorption coefficient spectrum into six Gaussian oscillators. (a) The resolved Gaussian peaks for initial guess #1. This fitting had a goodness of fit (GOF) value of 0.03. (b) initial guess #1. (c) Same as (a) using initial guess #2. This fitting had a GOF value of 0.03. (d) initial guess #2.

Figure S24 demonstrates that decomposing the non-contributing component of the absorption coefficient spectrum into seven Gaussian oscillators results in non-unique solutions that depend on the initial guess used. Hence, there is little confidence in these over-fits. However, all the center energies resolved using six Gaussian oscillators agree within 0.1 eV with the center energies resolved using seven Gaussian oscillators, implying that there is at least one oscillator centered at each presented energy in Figure 8, or a few oscillators around it.
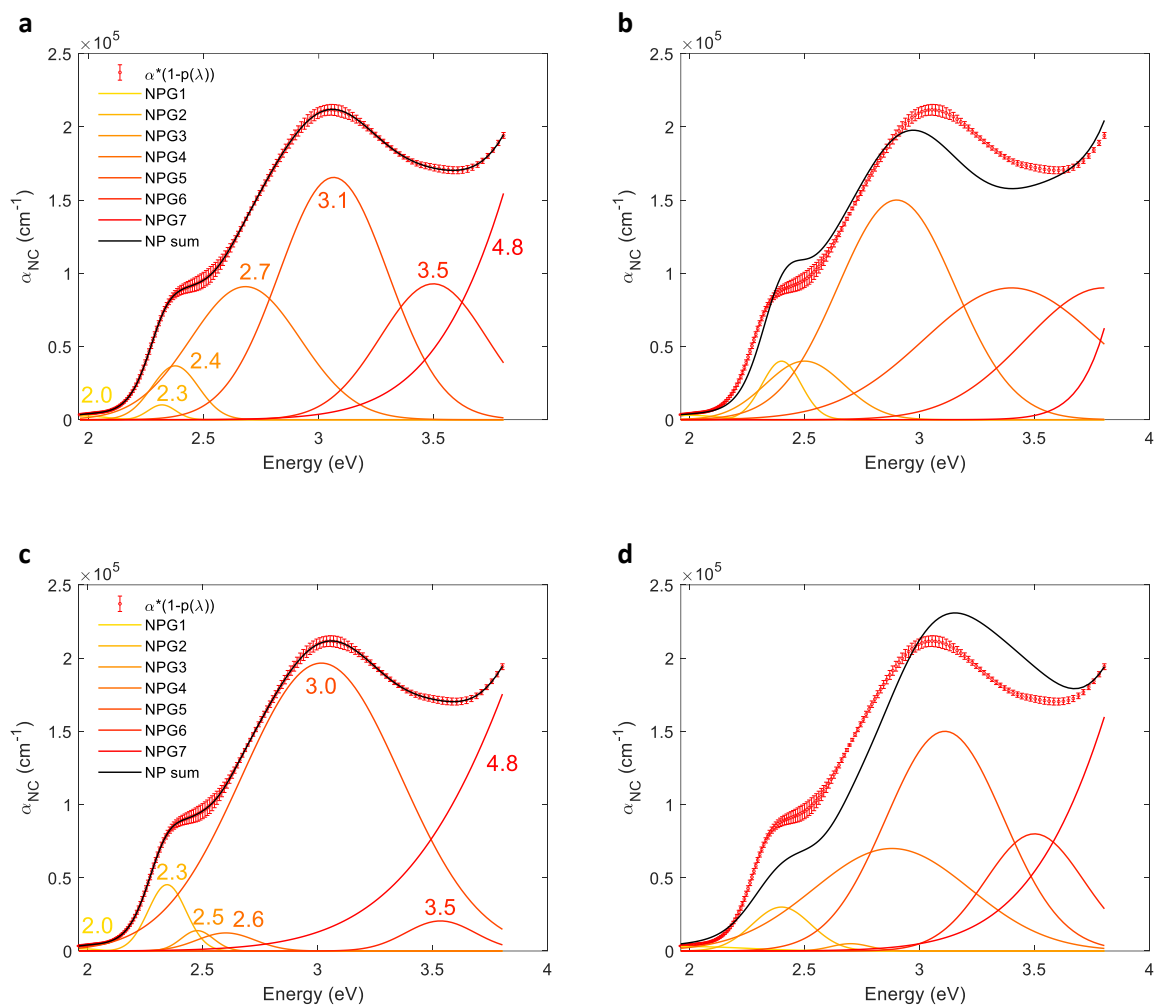
Figure S24. Resolving the non-contributing component of the absorption coefficient spectrum into seven Gaussian oscillators. (a) The resolved Gaussian peaks for initial guess #1. This fitting had a goodness of fit (GOF) value of 0.006. (b) initial guess #1. (c) Same as (a) using initial guess #2. This fitting had a GOF value of 0.004. (d) initial guess #2.
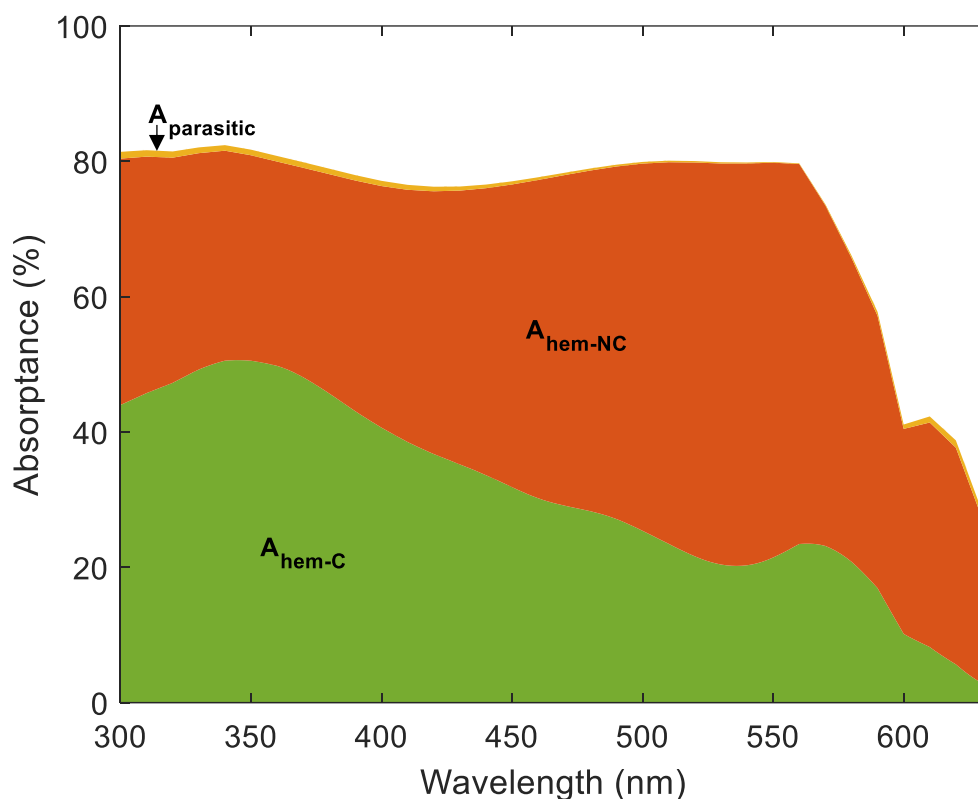
Performance estimations

Figure S25. Simulated sunlight absorption in a sample with a 1 μm thick hematite layer on a glass substrate with a 269 nm thick ITO layer. The contributing hematite absorptance (A_{hem-C}, green), non-contributing hematite absorptance (A_{hem-NC}, orange) and parasitic absorption in other components in the sample ($A_{parasitic}$, yellow). To calculate the contributing hematite absorption, the photogeneration yield spectrum $\xi(\lambda)$ was extrapolated linearly below 326 nm to reach the beginning of the AM1.5G sunlight spectrum.

Table S7. The maximal photocurrent in hematite, calculated for the AM1.5G sunlight spectrum from 300 to 592 nm. The theoretical photocurrent limit, considering all absorbed photons, and the maximal photocurrent, considering only the contributing photons that ultimately generate electrons and holes, in compact hematite layers of different thicknesses. The calculations were performed similarly to the described calculations in the main manuscript performed to produce Table 3.

Thickness	Maximal absorbed current (mA/cm^2)	Contributing photocurrent (mA/cm^2)		
		$\xi^1_{0.20}(\lambda)$	$\xi(\lambda)$	$\xi^1_{0.15}(\lambda)$
32 nm	5.0	1.8	2.1	2.5
100 nm	8.6	2.9	3.4	4.0
1 μm	12.1	3.9	4.5	5.3
10 μm	12.6	4.0	4.6	5.4
100 μm	12.6	4.0	4.6	5.4

Error Analysis

The EQE was calculated according to the following formula:

$$\text{EQE}(\lambda) = \frac{\#\,\text{holes}}{\#\,\text{photons}} = \frac{\frac{I\,[A]}{q\,[Cb]}}{\frac{OP\,[W]}{q\,[Cb]\cdot\frac{1240\left[\frac{eV}{nm}\right]}{\lambda\,[nm]}}} = \frac{1240\left[\frac{J}{Cb}\right]\cdot\Delta J_{ph}(\lambda)\,[A]}{\lambda\,[nm]\cdot OP(\lambda)[W]} \qquad \text{(Equation S3)}$$

where ΔJ_{ph} is the difference in the measured current with and without the monochromatic probe light, λ is the monochromator wavelength and OP is the optical power of the incident monochromatic probe light. Hence, the error of the EQE measurement (presented in Figure 3 in the article) was calculated based on the photocurrent measurement error, the optical power error and the wavelength error, according to the following formula:

$$\delta\big(\text{EQE}(\lambda)\big) = \text{EQE}(\lambda)\cdot\sqrt{\left(\frac{\delta\big(\Delta J_{ph}(\lambda)\big)}{\Delta J_{ph}(\lambda)}\right)^2 + \left(\frac{\delta(\lambda)}{\lambda}\right)^2 + \left(\frac{\delta(OP(\lambda))}{OP(\lambda)}\right)^2} \qquad \text{(Equation S4)}$$

The error of the current difference, $\delta\big(\Delta J_{ph}(\lambda)\big)$, was estimated by the standard deviation of six readings. The wavelength, $\delta(\lambda)$, error was estimated by the last digit of the wavelength reading (which is insignificant). The optical power error, $\delta(OP(\lambda))$, was estimated based on the accuracy of a power-meter reading at a certain wavelength (2% at the highest wavelength of the measured range) considering 30 readings were averaged and the squared-root dependency on the number of photons which vary with wavelength. The minimal error was assumed to be 0.1% of the measured EQE. This EQE error was considered in the fitting of the measured EQE, and therefore, in the extraction of the wavelength-dependent photogeneration yield and in the spatial collection efficiency.

The wavelength-dependent photogeneration yield of the thin (32 nm) film hematite photoanode, presented in Figure 5(b) in the article, was calculated by averaging the best six $\xi^1_{\bar{p}_m}(\lambda)$ corrected solutions as explained in the article. The range between the minimal and maximal spectra of the best six corrected solutions $\xi^1_{\bar{p}_m}(\lambda)$ (corresponding to $\bar{p}_m = 0.2$ and 0.15, respectively) is presented in colored area in Figure 5(b) in the article, and their standard deviation is presented by error-bars. Each $\xi^1_{\bar{p}_m}(\lambda)$ was obtained by averaging the corresponding sixfold corrected spectra, $\xi^{corrected}_{\bar{p}_m}(\lambda)$, presented in Figure S19.

The error in the photogeneration yield spectrum of the ultrathin (7 nm) film hematite photoanode was calculated as the standard deviation between the calculations for front and back probe illumination. The relative error of the calculated hematite absorption ($\frac{\delta A_{\text{hem}}}{A_{\text{hem}}}$) was estimated by the relative error of the whole sample calculated absorption ($\frac{\delta A}{A}$), since it is dominated by the hematite absorption. It was calculated by dividing the absolute value of the difference between the measured and calculated absorption by the measured absorption for both front and back probe illumination, and averaging the two. All the absorption calculations were performed using our optical modeling algorithm.[12] Since $A_{hem} \approx \alpha d$, where d is the hematite layer thickness, the attenuation relative error is also the same: $\frac{\delta \alpha}{\alpha} \approx \frac{\frac{1}{d}\delta A_{\text{hem}}}{\frac{1}{d}A_{\text{hem}}} \approx \frac{\delta A}{A}$. Considering $\alpha_C(\lambda)$ and $\alpha_{NC}(\lambda)$ are a simple multiplication of the attenuation coefficient by $\xi(\lambda)$ or $1-\xi(\lambda)$, they share the same relative error. Hence, the $\alpha_C(\lambda)$ error ($\delta \alpha_C$) is estimated by $\frac{\delta A}{A}\alpha_C$ and similarly the $\alpha_{NC}(\lambda)$ error ($\delta \alpha_{NC}$) is estimated by $\frac{\delta A}{A}\alpha_{NC}$. We used these error estimations for the calculations resolving

the contributing peaks presented in Figure 3, Figure 8, Table S6, Figure S19, Figure S23 and Figure S24.

References

1. Woollam, J. A. *et al*. Overview of variable-angle spectroscopic ellipsometry (VASE): I. Basic theory and typical applications. *Opt. Metrol. A Crit. Rev.* **10294**, 1029402 (1999).

2. Daniel A Grave, David S. Ellis, Yifat Piekner, Moritz Kölbach, Hen Dotan, Asaf Kay, Patrick Schnell, Roel van de Krol, Fatwa F. Abdi, Dennis Friedrich, A. R. Extraction of mobile charge carrier photogeneration yield spectrum of metal oxide photoanodes for solar water splitting. *Nat. Mater.* **20**, 833–840 (2021).

3. Chernyshova, I. V., Ponnurangam, S. & Somasundaran, P. On the origin of an unusual dependence of (bio)chemical reactivity of ferric hydroxides on nanoparticle size. *Phys. Chem. Chem. Phys.* **12**, 14045–14056 (2010).

4. Fondell, M., Jacobsson, T. J., Boman, M. & Edvinsson, T. Optical quantum confinement in low dimensional hematite. *J. Mater. Chem. A* **2**, 3352–3363 (2014).

5. Klotz, D., Ellis, D. S., Dotan, H. & Rothschild, A. Empirical in operando analysis of the charge carrier dynamics in hematite photoanodes by. *Phys. Chem. Chem. Phys.* **18**, 23438–23457 (2016).

6. Klotz, D., Grave, D. A. & Rothschild, A. Accurate determination of the charge transfer efficiency of photoanodes for solar water splitting. *Phys. Chem. Chem. Phys.* **19**, 20383–20392 (2017).

7.   Reference Solar Spectral Irradiance : "Air Mass 1.5 : Terrestrial Global 37 Deg South Facing Tilt" Spectrum Downloaded from Website : https://www.nrel.gov/grid/solar-resource/spectra-am1.5.html.

8.   Malviya, K. D. *et al.* Systematic comparison of different dopants in thin film hematite (α-Fe$_2$O$_3$) photoanodes for solar water splitting. *J. Mater. Chem. A* **4**, 3091–3099 (2016).

9.   Lunt, R. A., Jackson, A. J. & Walsh, A. Dielectric response of Fe2O3 crystals and thin films. *Chem. Phys. Lett.* **586**, 67–69 (2013).

10.   Nozik, A. J. PHOTOELECTROCHEMISTRY: APPLICATIONS TO SOLAR ENERGY CONVERSION. *Annu. Rev. Phys. Chem.* 189–222 (1978).

11.   Marusak, L. A., Messier, R. & White, W. B. Optical absorption spectrum of hematite, αFe2O3 near IR to UV. *J. Phys. Chem. Solids* **41**, 981–984 (1980).

12.   Piekner, Y. *et al.* Implementing Strong Interference in Ultrathin Film Top Absorbers for Tandem Solar Cells. *ACS Photonics* **5**, 5068–5078 (2018).

13.   Orton, J. W. and Powell, M. J. The Hall effect in polycrystalline and powdered semiconductors. *Rep. Prog. Phys.* **43**, 1263 (1980).